Geochimica et Cosmochimica Acta 404 (2025) 202–222

Contents lists available at ScienceDirect

Geochimica et Cosmochimica Acta

journal homepage: www.elsevier.com/locate/gca

Impact of silica on the identity of minerals formed in Archean oceans during Fe cycling by cyanobacteria and iron(III)-reducing bacteria

Carolin L. Dreher [a], Manuel Schad [b], Jan-Peter Duda [c], Stefan Fischer [d], Jeremiah Shuster [d,1], Yuhao Li [b], Kurt O. Konhauser [b], Andreas Kappler [a,e,*]

[a] Geomicrobiology, Department of Geosciences, University of Tuebingen, Tuebingen, Germany
[b] Department of Earth and Atmospheric Sciences, University of Alberta, Edmonton, Alberta, Canada
[c] Geobiology, Department of Geosciences, University of Goettingen, Goettingen, Germany
[d] Structural Microscopy Core Facility, Tuebingen University, Tuebingen, Germany
[e] Cluster of Excellence EXC 2124, Controlling Microbes to Fight Infection, University of Tuebingen, Germany

ARTICLE INFO

Associate editor: Juan Liu

Keywords:
Banded Iron Formations (BIF)
Iron redox processes
Microbial iron cycling
Nutrients

ABSTRACT

Banded Iron Formations (BIF) are iron- and silica-rich marine sediments deposited between 3.8 and 1.85 Ga. With the evolution of cyanobacteria, iron cycling via abiotic Fe(II) oxidation with O_2 produced by cyanobacteria and Fe(III) reduction by Fe(III)-reducing microorganisms is hypothesized to be responsible for BIF mineral deposition and transformation both in the water column and in the resulting sedimentary deposits. However, the impact of silica on iron mineralogy during microbially influenced iron cycling has not been determined experimentally under relevant ancient conditions. Hence, we set up batch incubation experiments with different concentrations of silica (0–2.2 mM) in the presence of varying concentrations of Fe(II) (0.5–5 mM), a marine cyanobacterium (*Synechococcus* sp. PCC 7002) and a marine dissimilatory Fe(III)-reducer (*Shewanella colwelliana*). We found that the fluctuation between microbial production of O_2 (cyanobacteria) and the activity of Fe (III)-reducing bacteria led to alternating Fe(II) oxidation and Fe(III) reduction and the precipitation of various Fe(II)- and Fe(III)-bearing minerals. Using a combination of X-ray diffraction and ^{57}Fe Moessbauer spectroscopy we identified poorly crystalline Fe(III)-bearing minerals (e.g., ferrihydrite), and the well crystalline ones (e.g., goethite, and lepidocrocite) in the absence of silica. Fe minerals precipitated in the presence of silica showed more pronounced reflections in μXRD, indicating higher crystallinity, while ^{57}Fe Moessbauer spectroscopy suggested the formation of Fe(II) silicate minerals and Fe(III) (oxyhydr)oxide minerals associated with silica. Furthermore, the presence of silica led to higher oxidation and reduction rates but more incomplete Fe(II) oxidation, while the reduction extent was higher in the presence of silica. In summary, our experiments showed that the presence of silica clearly affects Fe cycling and Fe mineral (trans)formation by cyanobacteria and Fe(III)-reducing bacteria, with relevance for the deposition of Precambrian Banded Iron Formations.

1. Introduction

Banded Iron Formations (BIF) are Precambrian marine sediments consisting of alternating silica (Si) and iron (Fe) oxide rich layers (Trendall and Blockley, 1970). They occur on every continent (Bekker et al., 2004; Konhauser et al., 2017; Ernst and Bau, 2021) and represent the largest iron ore deposits; e.g. the Hamersley Group in Australia contains 10^{13} tons of iron on an area of $\sim 10^5$ km^2 (Beukes, 1984; Trendall, 2002). BIF are categorized into two major groups based on their depositional environment: continental shelf deposits ("Superior-type": (Trendall, 2002)) and deposits associated with volcanic arc settings ("Algoma-type": (Konhauser et al., 2017)). The timing of the initial BIF deposition corresponds with the evolution of life 3.5 billion years (Ga) ago when the oceans were already teeming with diverse microbial life (for a review see Lepot (2020); for evidence from South Africa see Reinhardt et al. (2024) and Tice and Lowe (2004); for evidence from Australia see Duda et al. (2018), Mißbach et al. (2021) and Van Kranendonk (2011)), before the permanent rise of atmospheric oxygen

* Corresponding author at: Geomicrobiology, Department of Geosciences, University of Tuebingen, Tuebingen, Germany.
E-mail address: andreas.kappler@uni-tuebingen.de (A. Kappler).
[1] Now: Department of Earth Sciences, Western University, London, Ontario, Canada.

https://doi.org/10.1016/j.gca.2025.07.023
Received 20 March 2025; Accepted 23 July 2025
Available online 26 July 2025

known as the Great Oxidation Event (GOE) between 2.45 and 2.32 Ga (Bekker et al., 2004; Konhauser, 2011; Warke et al., 2020). Therefore, BIF mineralogy and geochemistry provide valuable information about environmental conditions and microbial processes during the time of their deposition.

BIF contain high amounts of silica (40–60 wt%) and iron (20–40 wt %) (Beukes, 1984; Trendall, 2002; Klein, 2005; Bekker et al., 2014; Konhauser et al., 2017), with an average iron oxidation state of 2.4 (Klein and Beukes, 1992). Typically, the silica rich bands consist of fine-grained quartz (chert), whereas the iron oxide rich layers are composed of a wide variety of minerals. In addition to iron oxides like hematite ($Fe_2^{III}O_3$) and magnetite ($Fe^{II}Fe_2^{III}O_4$), other typical Fe-rich minerals include iron carbonates such as siderite ($Fe^{II}CO_3$) and Fe^{II} silicates (Bekker et al., 2004, 2014; Klein, 2005). It is widely accepted that today's mineralogy reflects diagenetic and metamorphic overprints of the primary deposited minerals. In the water column, the primary mineral phases likely included ferric oxyhydroxides (e.g., ferrihydrite, $Fe(OH)_3$), ferrous silicates (e.g., greenalite, $(Fe^{II}, Fe^{III})_{2\text{-}3}Si_2O_5(OH)_4$), ferric silica gels, or ferrous carbonates (e.g., siderite, $FeCO_3$). Regardless of whether these minerals formed through biotic or abiotic pathways (see below), they were deposited on the seafloor forming BIFs (Han, 1966, 1978; Dimroth and Chauvel, 1973; Perry et al., 1973; Klein, 2005; Konhauser et al., 2005; Percak-Dennett et al., 2011; Wu et al., 2012; Zegeye et al., 2012; Rasmussen et al., 2014, 2015a,b; Sun et al., 2015; Alibert, 2016; Halevy et al., 2017; Johnson et al., 2018).

Prior to the GOE, oxygen produced as a byproduct of cyanobacterial metabolism would have been variable with concentrations ranging between 5 and 100 μM (Kasting, 1992; Kendall et al., 2010; Planavsky et al., 2010; Czaja et al., 2012). Similarly, Olson et al. (2013) estimated maximum concentrations of up to 10 μM oxygen in the seawater attributed to oxygen oases. These low oxygen concentrations enabled geochemical species to remain in solution in the slightly acidic to circumneutral seawater (Halevy and Bachan, 2017; Krissansen-Totton et al., 2018), e.g. the buildup of hydrothermally derived Fe^{2+} in the oceans (Jacobsen and Pimentel-Klose, 1988; Bau and Möller, 1993; Hamade et al., 2003) ranging from 0.02 to 0.5 mM (Holland, 1973; Morris, 1993). Silica was derived from the weathering of terrestrial sources and/or from hydrothermal processes in the oceanic crust, resulting in its accumulation in the seawater. The maximum ocean silica concentrations were controlled by the solubility of cristobalite (0.67 mM) and amorphous silica (2.2 mM) (Siever, 1992; Maliva et al., 2005), though Zheng et al. (2016) suggested slightly lower concentrations (0.5–1.6 mM).

Multiple abiotic and biotic processes have been proposed that fully or in part contribute to BIF mineral deposition. For example, highly depleted delta $\delta^{56}Fe$ in iron-rich bands of BIF (e.g. (Johnson et al., 2003, 2020; Czaja et al., 2013) and $\delta^{13}C$ values in Archean microfossils (Altermann and Kazmierczak, 2003; Tice and Lowe, 2004) are strong evidence for a microbial contribution. However, unambiguous microfossils have yet to be observed from BIFs (for a review see (Dreher et al., 2021)), which makes it necessary to discuss both abiotic and biotic processes. One abiotic process potentially contributing to Fe(III) mineral precipitation is the photochemical oxidation of Fe_{aq}^{2+} to Fe(III) by UV light (200–400 nm) (Cairns-Smith, 1978; Braterman et al., 1983). However, the significance of this process for BIF mineral formation was questioned since the effect of UV light would be attenuated by high concentrations of dissolved silica and/or bicarbonate within seawater (Konhauser et al., 2007). At the same time Fe(II) silicates (e.g. nontronite and chamosite) can form abiotically in the presence of dissolved Fe^{2+} and dissolved silica (Harder, 1978, 1976; Konhauser et al., 2007). Some authors considered abiotically precipitated greenalite ($(Fe^{II}, Fe^{III})_{2\text{-}3}Si_2O_5(OH)_4$) as the main primary mineral, which was then secondarily oxidized during diagenesis and metamorphism by hydrothermal fluids (Rasmussen et al. 2013, 2015b, 2019). However, greenalite forms at slightly alkaline pH values (7.5–8) (Beukes and Gutzmer, 2008; Tosca et al., 2016), contradicting the current assumption of circumneutral ancient ocean pH values (Halevy et al., 2017; Krissansen-Totton et al., 2018). However, Hinz et al. (2021) found greenalite precipitation at pH values of 6.5–7.0.

Among the processes potentially responsible for BIF mineral deposition, microbially driven iron redox processes are considered the most probable. The first hypothesis suggested that early cyanobacteria produced oxygen, leading to abiotic oxidation of dissolved Fe^{2+} to form Fe (III) (oxyhydr)oxide minerals (Cloud, 1965, 1973). This is in accordance with the widely accepted view that cyanobacteria caused the rise of free oxygen on Earth, leading up to the GOE (Holland, 2002; Bekker et al., 2004). However, this hypothesis does not explain the occurrence of early BIF, particularly as there is no direct evidence in BIF for the presence of cyanobacteria (see Schirrmeister et al., 2016 for a review). In these cases, phototrophic Fe(II)-oxidizing bacteria (photoferrotrophs) might have been responsible for the formation of most BIF minerals (Garrels et al., 1973; Hartman, 1984; Widdel et al., 1993; Konhauser et al., 2002; Kappler et al., 2005). This idea was further supported by the argument that photoferrotrophs were better suited for the nutrient-limited Archean ocean than cyanobacteria because of their lower need for phosphate (Jones et al. 2015).

Whether ferrous iron oxidation was indirectly influenced by cyanobacteria or directly by photoferrotrophic bacteria, Fe(III) (oxyhydr)oxides are produced; however, these minerals do not explain the existence of mixed-valent Fe(II)/Fe(III) minerals such as magnetite. Walker (1984) suggested that dissimilatory Fe(III)-reducing bacteria (DIRB) subsequently reduced the Fe(III) in Fe(III) (oxyhydr)oxides forming different Fe(II)-containing minerals that can be found in BIF today. This was supported by Konhauser et al. (2005) who calculated that as much as 70 % of the ferrihydrite produced in the water column would be converted back to Fe(II) via DIRB. Halama et al. (2016) subsequently demonstrated that diagenesis/metamorphism of Fe(III) minerals containing biomass (Fe(III) biominerals) produces Fe(II) phases but not magnetite. This implies that magnetite in BIF was likely formed via Fe (III) reduction by microorganisms.

Microbial laboratory studies are a powerful means to reveal the identity of BIF precursor minerals formed by Fe(II)-oxidizing and Fe(III)-reducing bacteria. A recent study combined phototrophic Fe(II)-oxidizing bacteria (*Chlorobium N1*) and anaerobic Fe(III)-reducing bacteria (99 % sequence similarity to *Shewanella colwelliana*) to determine BIF precursor minerals (Laufer et al., 2016) for three consecutive redox cycles in Fe(II)- (up to 5 mM) and silica-rich (up to 1.5 mM) artificial sweater medium (Schad et al., 2022). In these experiments, ferrihydrite, goethite and possibly Fe(II)-bearing silicates were formed albeit no magnetite was detected. At the same time, Nims and Johnson (2022) showed that goethite and layered Fe(II)-bearing silicates, most likely greenalite, were formed by the biotic reduction of synthesized ferrihydrite by the dissimilatory Fe(III)-reducing bacterium *Shewanella putrefaciens* CN32. The effect of photoferrotrophs and Fe(III)-reducing bacteria on the mineralogy is increasingly well understood but the effect of cyanobacteria and differing Si concentration remains underexplored. Most importantly, the impact of different silica concentrations (0.67–2.2 mM) on both the activity of O_2-producing cyanobacteria and Fe(III)-reducing bacteria (specifically, on the rates and extent of Fe(II) oxidation and Fe(III) reduction), as well as on the resulting mineral identity, has also not been investigated to date.

In this study, we explored the potential impact of silica on microbial Fe cycling and associated mineral (trans)formation processes on the juvenile Earth. More specifically, we co-cultivated marine cyanobacteria (strain *Synechococcus* sp. PCC 7002) with dissimilatory Fe(III)-reducing bacteria (strain *Shewanella colwelliana*) in three subsequent redox cycles under mimicked Precambrian ocean water column conditions. The experiments were conducted in controlled bottle experiments instead of flow-through systems to simplify the setup and enable precise control over geochemical variables such as iron and silica concentrations. In the water column, cyanobacteria inhabit the photic zone where they slowly oxidize Fe(II), while microbial Fe(III) reduction typically occurs in

deeper, anoxic zones. The co-culturing of cyanobacteria and *Shewanella* is justified by the latter's facultative metabolic versatility: *Shewanella* can perform aerobic respiration in the presence of oxygen and switch to either fermentation or Fe(III) reduction under anoxic conditions. Furthermore, within cell-mineral aggregates that form from cyanobacterial biomass and biogenic Fe(III) minerals, localized anoxic microhabitats can develop – even in otherwise oxic or microoxic conditions – also allowing Fe(III) reduction *in situ*. Building on the work of Schad et al. (2022), we determined the influence of different silica concentrations on iron mineral (trans)formation as well as on Fe(II) oxidation and Fe(III) reduction rates by analyzing wet-chemical Fe speciation, dissolved silica and oxygen concentrations, and cell counts. The precipitated minerals and cell-mineral aggregates were analyzed using ^{57}Fe Moessbauer spectroscopy, X-ray diffraction (XRD) and scanning electron microscopy coupled with energy dispersive spectrometry (SEM-EDS). The overall goal of this study is to understand the effects of silica on microbial processes and associated iron mineral (trans-) formations.

2. Material and methods

2.1. Cultivation of microorganisms and growth conditions

A culture of the cyanobacterium *Synechococcus* sp. PCC 7002 was provided by Gen Enomoto from the University of Freiburg and was cultivated in liquid, autoclaved, oxic A+ medium. This medium was composed of five different stock solutions made using MilliQ water. The volume and composition of each stock were as follows. Stock 1 (2 mL, diluted 1:2) contained 3.89 g/L $FeCl_3$*$6H_2O$, 34.3 g/L H_3BO_3, 4.3 g/L $MgCl_2$*$4H_2O$, 0.315 g/L $ZnCl_2$, 0.03 g/L MoO_3, 0.003 g/L $CuSO_4$*$5H_2O$, 0.0122 g/L $CoCl_2$*$6H_2O$. Stock 2 (10 mL) contained 100 g/L Trizma base adjusted with HCl to pH 8.2. Stock 3 (100 mL) contained 0.5 g KH_2PO_4, 10 g/L $NaNO_3$, 24.4 g/L $MgSO_4$, 180 g/L NaCl, 6 g/L KCl. Stock 4 (10 mL) contained 0.3 g/L Na_2EDTA. Stock 5 (10 mL) contained 2.8 g $CaCl_2$. The PCC 7002 culture was grown until a cell density of ~10^8 cells/mL at 25 °C in an Erlenmeyer flask on a shaker (60 rpm) in day-night cycles (12/12) under a halogen 40-Watt light bulb with an intensity between 300 and 500 lx. *Synechococcus* sp. PCC 7002 is not situated close to the base of the phylogenic tree of cyanobacteria (Schirrmeister et al., 2015). All modern cyanobacteria do not stem from a comparable low nutrient environment like the early oceans, so this stain was chosen as a model organism because it is well-studied and shows fast and stable doubling rates.

The dissimilatory Fe(III)-reducing bacterium *Shewanella colwelliana* (obtained from the German Collection of Microorganisms and Cell Cultures GmbH (DSMZ)) was cultivated on DSM 514 agar plates (Bacto Marine Broth DIFCO 2216), which contained 15 g/L Agar, 5 g/L Bacto™ peptone, 1 g/L bacto yeast extract, 0.1 g/L Fe(III) citrate, 19.45 g/L NaCl, 5.90 g/L $MgCl_2$, 3.24 g/L Na_2SO_4, 1.80 g/L $CaCl_2$, 0.55 g/L KCl, 0.16 g/L $NaHCO_3$, 0.08 g/L KBr, 0.34 g/L $SrCl_2$, 22 mg H_3BO_3, 0.04 g/L Na-metasilicate·$9H_2O$, 0.024 g/L NaF, 1.60 g/L $(NH_4)NO_3$, 8 mg Na_2HPO_4. The pH was adjusted to 7.14 using HCl prior to sterilization via autoclaving. These cultures were incubated at 25 °C.

We chose *Shewanella colwelliana* as the Fe(III)-reducer because it is a well-studied marine microorganism that has been previously used in experiments simulating iron cycling in ancient ocean analogues Schad et al. (2022). Importantly, *S. colwelliana* exhibits metabolic flexibility, allowing it to tolerate and adapt to the presence of oxygen – an essential trait for our experimental setup involving oxygen-producing cyanobacteria. In the presence of oxygen, however, its capacity for Fe(III) reduction is suppressed, as it preferentially utilizes oxygen as the terminal electron acceptor (von Canstein et al., 2008; Lassak et al., 2010; Zhang et al., 2013). The cyanobacterium *Synechococcus* sp. PCC 7002 was chosen for its well-documented physiology, its robust growth in seawater, and efficient oxygen production, making it particularly suitable for our experimental setup.

2.2. Setup of the iron cycling experiments

The aim of these experiments was to investigate the resulting mineralogy after alternating Fe(II) oxidation by cyanobacterially produced oxygen and microbial Fe(III) reduction representing a simplified model of the early Archean ocean to investigate the mineralogy after three subsequent Fe(II) oxidation and Fe(III) reduction cycles. To this end, the planktonic cyanobacterium *Synechococcus* sp. PCC 7002 and the Fe(III)-reducer *Shewanella colwelliana* were cultured together in anoxic artificial seawater medium (ASW, see details below) containing different concentrations of dissolved ferrous iron (0, 0.5, 1, 2.5 and 5 mM) and dissolved monomeric silica (0, 0.67 and 2.2 mM). To promote microbially induced Fe(II)-oxidizing and Fe(III)-reducing conditions, the bottles were intermittently exposed to light and darkness to have three complete redox cycles. All experiments were conducted in 250 mL-volume Schott bottles and performed in triplicates.

For the experimental bottles, artificial seawater (ASW) was prepared anoxically using MilliQ water, dissolved salt solution (i.e., 17.3 g/L NaCl, 8.6 g/L $MgCl_2$·$6H_2O$, 0.025 g/L $MgSO_4$·$7H_2O$, 0.99 g/L $CaCl_2$·$2H_2O$, 0.39 g/L KCl, 0.059 g/L KBr, 0.05 g/L KH_2PO_4, 0.25 g/L NH_4Cl, 2 g/L $NaHCO_3$), and silica concentrations as previously mentioned. Note, the salts, bicarbonate buffer (30 mM), and monomeric silica stock solution were purged with N_2 (the buffer with N_2/CO_2 (90 vol%/10 vol%)) and separately autoclaved. Immediately after autoclaving, a Widdel flask containing the salt solution was flushed with N_2/CO_2; while it was still hot (~70–80 °C), the sterile silica solution was added. Upon mixing the two solutions, white flocs formed. The medium was allowed to cool to 20 °C, the bicarbonate buffer was added, and the pH was adjusted to 7 using 1 M anoxic HCl. Because of the precipitates (i.e., white flocs), the medium was distributed in 2 L-volume Schott bottles and kept at room temperature for two days allowing the precipitates to settle to the bottom of the bottle. After settling, the medium was filtered using a 0.22 μm-pore size PES Bottle-top-filter in the glovebox. Vitamins and trace element solutions were added under sterile conditions at the bench and the pH was readjusted to pH 7 using HCl. Using a constant stream of N_2/CO_2 to maintain anoxic conditions, aliquots (100 mL) of the prepared medium were dispensed into sterile 250 mL-volume Schott bottles. Oxygen concentrations were monitored over time (see 2.2.5 below) and any bottle containing more than 3 μM oxygen was flushed with N_2/CO_2 to maintain anoxic conditions. An anoxic 100 mM or 1 M stock solution of $FeCl_2$ was added aseptically to each Schott bottle and pH was remeasured to ensure it remained circumneutral (pH 7). During the entire course of the experiments, the pH values did not exceed 7.5.

Grown cyanobacteria were washed three times with ASW prior to being inoculated into the Schott bottles to a final cell density of 10^6 cells/mL. After the termination of the first oxidation half-cycle, the bottles were wrapped in aluminum foil to arrest photosynthesis and purged with N_2/CO_2 until the dissolved O_2 concentration was below 3 μM. Grown *Shewanella colwelliana* cells were suspended and washed three times with ASW and then added to a final concentration of 10^6 cells/mL. To induce Fe(III) reduction, lactate ($C_3H_5O_3$) was added as electron donor with a concentration calculated to reach 70 % Fe(III) reduction (Reaction (1)). Lactate was added as the electron donor for the Fe(III)-reducers because simple test experiments (not shown) showed that the Fe(III)-reducer cannot directly use the cyanobacterial biomass as electron donor without the support by a fermenting and thus biomass-degrading microbial community. This corresponds closely to the previous experimental work by Rico et al. (2023) who similarly documented a lack of growth by *Shewanella oneidensis* MR-1. After 70 % Fe(III) reduction, the bottles were unwrapped and placed back into light to promote photosynthesis.

$$8\,H^+ + 4\,Fe(OH)_3 + C_3H_5O_3^- \leftrightarrow 4\,Fe^{2+} + 10\,H_2O + CH_3COOH + HCO_3^- \quad (1)$$

2.3. Quantification of Fe(II) and Fe(III) by the spectrophotometric Ferrozine assay

The ferrozine assay is a spectrophotometric method in which the ferrozine molecule binds to Fe^{2+} and forms a purple complex, which can then be quantified by its absorption at 562 nm (Hegler et al., 2008). Aliquots (100 μL) of fluid phase were sampled from each bottle. The slurry samples were first dissolved and diluted in 1 M HCl to a concentration of up to 1 mM Fe. For Fe^{2+} analysis, 80 μL of 1 M HCl were pipetted into a 96-well plate followed by adding 20 μL sample. After 15 min of incubation, 100 μL ferrozine solution was added and after 5 min of incubation, the samples were analyzed at 562 nm using a Thermo Fisher Scientific (USA) MultiskanTM GO Microplate Spectrophotometer plate reader. The total iron ($Fe_{(tot)}$) determination procedure varies by the addition of 80 μL of 10 % (w/v) of the reducing agent hydroxylammonium hydrochloride (HAHCl) instead of HCl prior to the sample addition and a longer incubation time of 30 min. Standards between 0 and 1000 μM were used to calculate the iron concentration.

2.4. Quantification of dissolved silica by the molybdenum blue method

Dissolved silica, including monomeric silica and colloidal silicic acid (Si-colloids), were quantified using the Molybdenum Blue Method (Fanning and Pilson, 1973). Briefly, slurry samples were sampled using a syringe, filtered (0.22 μm-pore size PES) and diluted in MilliQ to 1 mL. 40 μL of an ammonium heptamolybdate tetrahydrate (6.33 g/50 mL H_2O) in a 4.5 M sulfuric acid solution were added to form a blue complex with the silica. To avoid complexing with phosphate, 40 μL of an oxalic acid solution was added. Lastly, 20 μL of ascorbic acid was added as a reductant. After 30–60 min of incubation, the blue silica-molybdenum complexes were quantified at 810 nm. Different standards between 1 and 100 μM were used to calculate the silica concentration.

2.5. Oxygen quantification by optode sensors

Dissolved oxygen concentrations were measured with a luminophore optode foil from PreSens (Germany). 3 × 3 mm pieces of foil were attached using silicon glue in the lower 2 cm of each bottle to ensure contact with the liquid phase. The collision of the optode foil (luminophore) and the quencher (oxygen molecules) leads to an energy transfer from the foil to the oxygen which leads to the decrease of luminescence signal of the foil. The oxygen concentration in the liquid phase can then be calculated using the Stern-Volmer-equation. The attached temperature sensor was placed into a Schott bottle co-incubated under the same conditions as the experiments. For each container and each set of optode foil a new two-point calibration was conducted prior to the measurements, one at complete oxygen saturation, one at oxygen-free conditions. To measure the first calibration point, 100 mL pure ASW medium was filled into a 250 mL Schott bottle with an optode foil and stirred vigorously until complete O_2 saturation. Subsequently, 10 % w/v sodium dithionite ($Na_2S_2O_3$) was added to reduce all O_2 remaining in solution and the second calibration point was measured.

2.6. Mineral analysis by micro X-ray diffraction (μXRD)

A Bruker's D8 Discover GADDS XRD2 micro-diffractometer equipped with a standard sealed tube with a Co-anode (1.78897 Å) at parameters of 30 kV/30 mA was used to perform X-ray diffraction analysis for the identification of crystalline mineral phases. Low-weight (mg-range) samples were sampled, dried and ground in an anoxic chamber and loaded onto silicon wafers. The double reflection angle (2 theta) of the emitted X-rays was detected in a range from 10° to 70° 2 theta in 240 s. To assign the mineral phases, we identified the three most prominent mineral reflection signals in the Match! Software from Crytal Impact, Germany. Due to the overlaps of the various mineral phases in the middle angles and the high background because of the high biomass concentrations, we looked at the most prominent reflection line first.

2.7. Analysis of cell-mineral aggregates by scanning electron microscopy coupled to energy-dispersive spectroscopy

Before sampling, each experimental bottle was gently agitated to evenly disperse suspended cells and minerals within the fluid phase. At the end of the third redox cycle, an aliquot (900 μL) was sampled from each bottle and placed into a 1 mL-volume Eppendorf tube. Electron microscopy-grade glutaraldehyde (25 %) was added to each sample for a final 2.5 % concentration. The tube lids were closed, wrapped with parafilm to avoid contamination or spillage, and agitated using a vortex mixer to evenly disperse cells in the fixative solution. The samples were incubated for at least 24 h at 4 °C to allow bacterial cells to be thoroughly fixed. After incubation, the tubes were centrifuged (10,000 g for 1 min) to form a cell-mineral pellet and the supernatant of the fixative solution was removed. Filter sterile (0.45 μm pore size) deionized water was added to each tube and the lids were closed prior to resuspending the cells and minerals in the fluid phase by vortex. An aliquot (ca. 50 μL) of each sample was placed onto poly-L-lysine coated glass slides that were prepared in advance. Briefly, 25 μL of 0.01 % poly-L-lysine solution was placed onto cleaned and hydrophilic 12 mm diameter glass slides (i.e., glass slides washed with RBS cleaning solution and glow discharged for 25 sec at 0.39 mbar in a PELCO easiGlow). To dry the poly-L-lysine on the glass slides, the slides were placed in a 50 °C incubator for 1 h. Once dry, individual coated slides were placed at the bottom of individual wells of a 24 well-plate. Cells and minerals were allowed to settle onto the poly-L-lysine coating over a 15 min incubation period, with the well-plate lid closed. The samples were dehydrated using increasing concentrations of ethanol. First, ca. 1 mL of 25 % ethanol was added to each sample-containing well and incubated for 15 min at room temperature (ca. 21 °C) after which most of the ethanol solution was removed. This dehydration procedure was repeated with 50, 75, and (3×) 100 % ethanol with 15 min incubations for each concentration. A solution containing a 1:1 ratio of 100 % ethanol and hexamethyldisilazane (HMDS) was then added to each well and incubated for 30 min. The ethanol-HMDS solution was removed after incubation, immediately replaced with 100 % HMDS, and incubated for an additional 30 min, with the well-plate lid closed. Before the final incubation, fresh HMDS was added and then the well-plate lid was placed ajar to allow the HMDS to evaporate overnight. Once dry, each sample was attached to a 12 mm diameter aluminum stub using carbon adhesive tabs (Plano GmbH). The samples were coated with ~8 nm of gold using a BAL-TEC SCD 005 sputter coater to prevent charging during scanning electron microscopy analysis. The samples were imaged in Secondary Electron (SE) mode using a Zeiss Crossbeam 550L Focused Ion Beam (FIB) – Scanning Electron Microscope (SEM) operating with an acceleration voltage of either 2 or 15 kV with a working distance of 5.1–5.2 mm. Elemental spectra were obtained using either spot or region analysis using an Oxford Instruments Energy Dispersive Spectrometer (EDS) (UltimMax 100) and an acceleration voltage of 15 kV. The spectra were analyzed using Oxford Instruments' AZtec software.

2.8. Determination of the cell numbers by hemocytometry

At the start and end of each redox half-cycle, the cell density was counted using a Leica CTR 5500 microscope (400× magnification), a Neubauer-improved hemocytometer from Hirschmann, and a 10 μL sample. Cells were counted within 100, 0.05 × 0.05 mm squares and the total number was multiplied by the dilution factor (2.5×10^7) to obtain the cell count in mL/L. Cell morphology (i.e., cocci- vs. rod-shaped), size (i.e., 1 μm diameter in all directions vs. 1 μm length to 0.1 μm width) and autofluorescence were used to differentiate between cyanobacteria and DIRB.

2.9. Moessbauer spectroscopy

Three different samples, collected from setups containing 2.5 mM iron without silica and 5 mM iron but varying silica concentrations ranging from 0 mM ('no silica'), to 0.67 mM ('low silica') and 2.2 mM ('high silica'), were analyzed by Moessbauer spectroscopy. The samples were taken after three respective redox cycles at the end of the experiments. Additionally, samples from a Fe(II) oxidation experiment containing 1 mM iron were prepared. Due to the high density of the cells, the solid iron concentrations of the 0.5-, 1- and some 2.5-mM iron experiments were too low to be measured by ^{57}Fe Moessbauer spectroscopy. The samples analyzed were still at the lower limit of iron concentration necessary, thus explaining the high background. ^{57}Fe Moessbauer spectroscopy allows the quantification of Fe(II)- and Fe(III)-phases in solids mineral phases. The gamma-rays of a constantly moving radioactive Rhodium-embedded ^{57}Co source are resonantly adsorbed by the nuclei of ^{57}Fe in the sample. The resulting hyperfine interaction in the magnetic and electric field of the magnetic field is then displayed in a transmission spectrum. The measurements are typically conducted at temperatures from room temperature (298 K) to 5 K. Fe-bearing phase undergo magnetic ordering during the cooling process which is indicated by the transformation of doublets to sextet spectra. By comparing the spectra at different temperatures information about the phase identity, crystallinity and crystal size can be drawn.

Several 0.45 μm syringe filters were loaded with slurry sample material in the glovebox and up to three filters were then stacked and glued between Kapton tape. The samples were then stored anoxically at −25 °C until measurement. Samples were measured at 77 K and 5 K and the spectra fitted using the extended Voigt based fitting (xVBF) in the Recoil software (University of Ottawa, Canada). The instrument was calibrated by using a ^{57}Fe foil. The linewidth of 0.124 mm/s, determined from the minimum inner line broadening from the calibration foil, and the relative peak areas (3:2:1:1:2:3) were fixed during fitting. All mineral phases are mainly defined by the center shift (CS) in mm/s, doublets also by the quadrupole splitting (QS) in mm/s, an indicator for the distance of the two peaks. Sextets are additionally defined by ε in mm/s, a parameter describing the asymmetry of the sextet and by the hyperfine field (H) in T, the spreading of the peaks. The standard deviation (stdev) in T is an indicator for the wideness of the peaks, therefore also an indicator of crystallinity: the more crystalline, the smaller the stdev. Very crystalline and magnetically ordered phases appear as sextet from room temperature on, whereas non-magnetic, non-crystalline phases appear as doublets at 5 K.

3. Results

3.1. Effect of Si on Fe cycling by cyanobacteria and Fe(III)-reducing bacteria at low Fe concentrations (0.5 and 1 mM Fe)

We tracked concentrations of total iron, $Fe(II)_{total,}$ dissolved silica

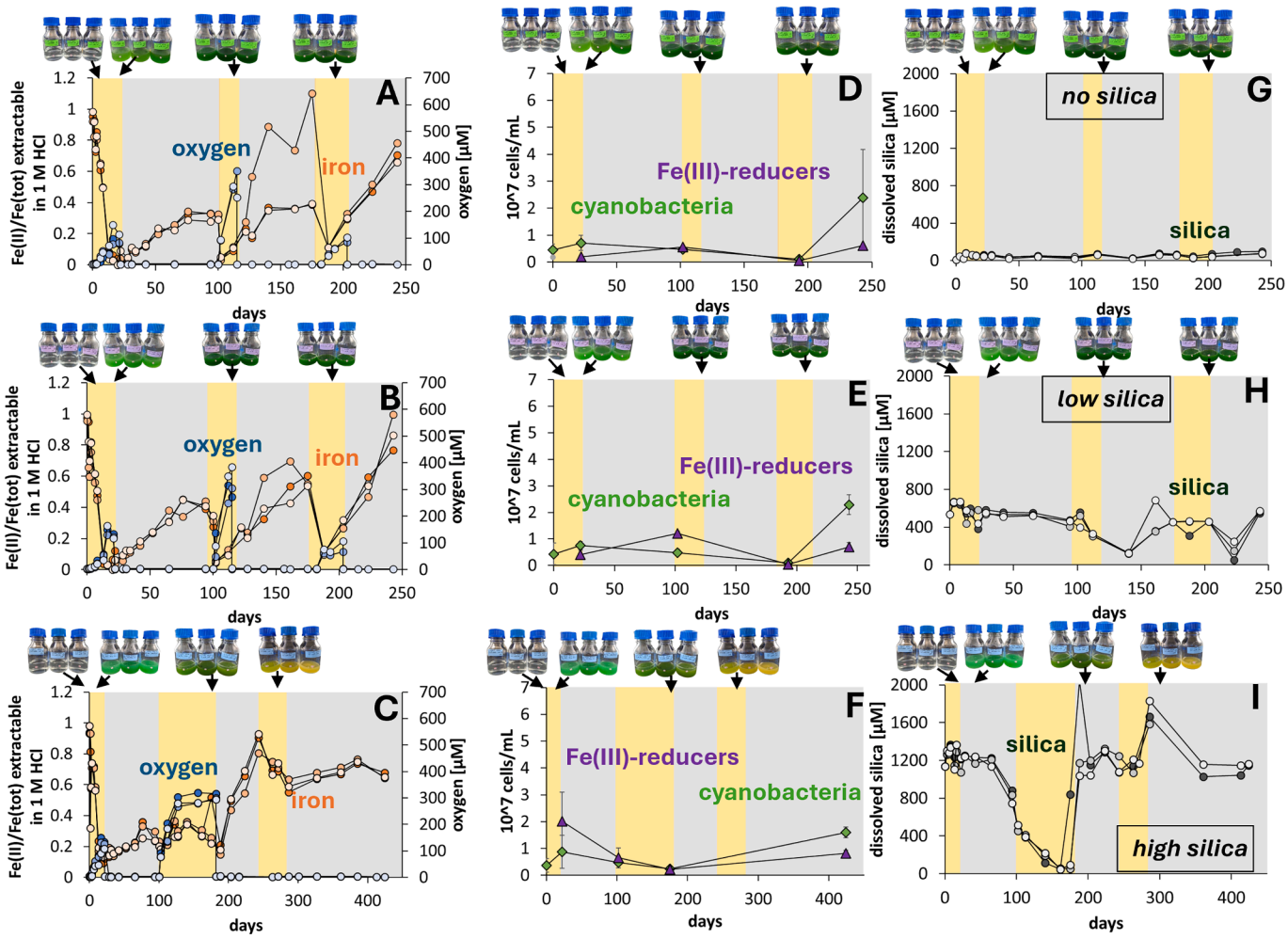

Fig. 1. Cycling experiments with 0.5 mM Fe(II) and 0, 0.67 and 2.2 mM added silica. Left panels show Fe(II)/$Fe_{(tot)}$ ratios (orange) and oxygen concentrations (blue). The panels in the middle column show cell counts (and standard deviation) of the cyanobacteria (green) and Fe(III)-reducers (purple) while the right columns show dissolved silica concentrations. The yellow background indicates periods of Fe(II) oxidation, while the grey background shows periods of Fe(III) reduction. The photographs on top show the triplicate bottles in the beginning of the experiment and at the end of each of the three oxidative half-cycles.

and number of cells of the cyanobacteria and Fe(III)-reducing bacteria over three subsequent oxidation and reduction cycles. The first part of the results describes the effect of silica on iron cycling in bottles containing either 0.5 and 1 mM initially added Fe(II) ('low iron experiments') (Figs. 1 and S1). The data presented here is from the 0.5 mM iron experiments which present the dissolved iron concentration most similar to estimated concentrations for Archean seawater (Holland, 1973; Morris, 1993). The data for the 1 mM iron experiments show very similar trends and can be found in the supporting information.

3.1.1. *Influence of silica on Fe(II) oxidation during Fe redox cycling at low Fe concentrations*

No distinct differences in Fe(II) oxidation rates were observed from bottles containing cyanobacteria grown in the absence ('no silica') or in the presence of 0.67 mM of silica ('low silica') (Figs. 1A and B; 2; Table S1). In the first oxidation half-cycle, Fe(II) was fully oxidized in the 'no silica' setups (30–33 μM/day), while the oxidation reached <99 % in the 'low silica' setups (23–25 μM/day). The second half-cycle reached ~94 % Fe(II) oxidation in two days in both setups (~62–87 μM/day), while in the third half cycle Fe(II) was oxidized to ~90 % in both setups (14–46 μM/day). Fe(II) oxidation rates were diminished in the presence of 2.2 mM Si ('high Si') (Fig. 1): full Fe(II) oxidation was inhibited in the first half-cycle (maximum Fe(II) oxidation of 90 %; 28–30 μM/day). In the second half-cycle, we no longer observed Fe(II) oxidation. Instead, the Fe(II)/$Fe_{(tot)}$ ratio fluctuated around 30 %, while in the third half-cycle only 20 % of the iron(II) was oxidized (0–2 μM/day).

The bottles initially containing 1 mM Fe(II) had Fe(II) oxidation rates that were approximately twice as high as the ones which contained 0.5 mM Fe(II) (Fig. S1). Similar to the experiments with 0.5 mM initial Fe(II), the oxidation rates and extent in the 'no silica' and in the 'low silica' setups showed very similar trends (almost complete oxidation; Fig. S1A and B, respectively), while Fe(II) oxidation in 'high silica' conditions was negatively affected, resulting in incomplete Fe(II) oxidation and lower oxidation extents with ongoing cycling (Figs. S1C and 2; Table S1).

3.1.2. *Influence of silica on O_2 production, accumulation of O_2 and cell counts at low Fe concentrations*

The production and accumulation of oxygen in the fluid phase of bottles containing low iron and 'no silica' or 'low silica' were similar during the illuminated stage (Fig. 1A and B). At the end of the first half-cycle (22 days), the oxygen concentration in the liquid reached around 100 μM. In both the 'no silica' and 'low silica' setups, oxygen started rising exponentially after a lag phase of six days. During the second half-cycle, the accumulated dissolved oxygen increased to 400 μM. Finally, the third half-cycle showed oxygen concentrations up to 100 μM.

In the 'high silica' setups (Fig. 1C), oxygen concentrations in the 0.5 mM iron experiments developed similarly compared to the 'no silica' and 'low silica' setups during the first half-cycle. However, during the second half-cycle, even though the dissolved oxygen also accumulated to 400 μM, in contrast to the 'no silica' and 'low silica' setups, it did not lead to measurable Fe(II) oxidation. In the third half-cycle of the 'high silica' setup, we did not measure dissolved oxygen. During the reduction periods, the oxygen values always stayed <5 μM at all silica concentrations tested.

During the illumination (oxidation) periods, in all three setups ('no silica', 'low silica' and 'high silica'), the contents of the bottles turned orange during the first three days and then quickly changed to green. The green color was a phenotypic indication of high cyanobacterial cell density and correlated well with the rapidly increasing oxygen concentrations at the beginning of each oxidation period. The number of cyanobacterial cells during the three oxidation cycles showed similar trends, independent of the silica concentrations. The initial number of 2–3*10^6 cells/mL doubled in the first oxidation half-cycle and reached highest values of 3*10^7 cells/mL after three oxidation cycles (Fig. 1D–F).

Compared to the 0.5 mM Fe(II) experiment, the 1 mM experiment showed lower oxygen concentrations in the 'no silica' and in the 'low silica' setups (100–400 μM and 50–300 μM respectively; Fig. S1A and B). The 'high silica' setup showed maximum oxygen concentrations of 600 μM in the first half-cycle (Fig. S1C). The cell counts were very similar to the 0.5 mM experiment, only the 'low silica' setup with 1 mM Fe(II) showed slightly higher cell counts (up to 5*10^7 cells/mL) than the 0.5 mM iron equivalent (3*10^7 cells/mL).

3.1.3. *Influence of silica on Fe(III) reduction during Fe redox cycling at low Fe concentrations*

For the reductive periods of the redox cycling incubations, we calculated the Fe(III) reduction rates considering only the phases of active reduction and left out lag phases at the beginning or the end of the

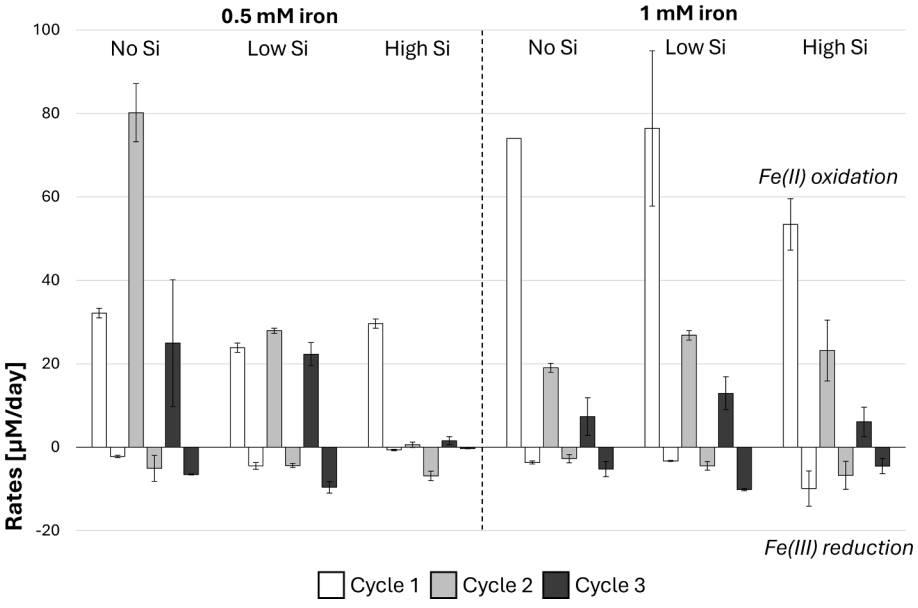

Fig. 2. Fe(II) oxidation (positive values) and Fe(III) reduction rates (negative values) in the three oxidative half-cycling experiments (white, grey, dark grey) with low initial Fe(II) concentrations (0.5 and 1 mM).

reductive period. Overall, the Fe(III) reduction rates were lower than the Fe(II) oxidation rates (Fig. 2; Table S2) and we did not detect a considerable impact of the silica concentration. In the 'no silica' and 'low silica' setups (Fig. 1A and B), the reduction half-cycles took between 50 and 80 days at reduction rates of ca. 2–4 μM/day. In the 'no silica' setup the percentage of Fe(II) increased from 40 to 80 % from the first to the third cycle, while the time until a stable Fe(II) concentration was achieved decreased from 80 to 50 days. The reduction rate, therefore, rose from 2 μM/day to 10 μM/day from the first to the third reductive half cycle. The 'low silica' setup showed an increase in the reduction extent from 40 % after 80 days to 90 % after 50 days with ongoing cycling, which translates to reduction rates from 3 μM/day to 11.5 μM/day. In the 'high silica' setup (Fig. 1C), the reduction extent increased and the reduction rates became faster from 40 % (3–5 μM/day) during the first half-cycle to 80 % (8–12 μM/day) during the second cycle, respectively, and then remained consistent with 60–80 % Fe(II)/$Fe_{(tot)}$ during the last cycle (reduction rate of ca. 8–12 μM).

The 'no silica' and 'low silica' setups initially containing 1 mM Fe(II) (Fig. S1A and B) showed lower Fe(III) reduction extents than the 0.5 mM Fe(II) experiment (maximum 50 % compared to 100 %), while the reduction rates (<11 μM/day) were comparable to the 0.5 mM experiment (Table S2). However, in the 'high silica' setup (Fig. S1C) the reduction extent increased to 80 % and the silica stimulated the reduction rates to values of up to 16 μM/day.

3.1.4. Influence of silica concentration on Si mobility during Fe redox cycling at low Fe concentrations

The 'no silica' setups showed constant silica values of <80 μM (Fig. 1G), probably stemming from lab ware used such as glass bottles. In the 'low silica' and 'high silica' setups, the dissolved silica initially was 500 and 1100 μM, respectively, and then increased within the first three days by ~80 μM (Fig. 1H and I). The highest dissolved silica concentrations measured in the 'low silica' setup was 685 μM during the second reduction phase, which corresponded well to the calculated added concentration of 670 μM. During the first 140 days, the dissolved silica decreased to 120 μM. The Fe(II)/$Fe_{(tot)}$ ratio varied between 30 and 60 %, so over 500 μM silica were either precipitated as silica mineral flocs or associated with Fe(II) and Fe(III) minerals. Overall, the oxidation or reduction cycles did not show distinct silica cycling, but during the second and third reduction half cycle, silica precipitated temporarily but mostly went back into solution. The 'high silica' setups showed a maximum dissolved silica concentration of between 1600 μM and 2000 μM at the end of the second and third oxidation half cycle. This indicated that between 200 and 600 μM of silica formed flocs or were associated with particles that were filtered out before starting the experiment. During the first oxidation half-cycle about 1400 μM of silica stayed in solution, whereas at the end of the first reduction half-cycle we measured 1200 μM dissolved silica. In the subsequent second oxidative half-cycle, all silica was removed from solution, which means that ~2000 μM of silica were associated with ca. 400 μM of solid Fe(III) and 100 μM of Fe(II). During the second reduction period, dissolved silica concentrations reached again 1200 μM. In the third oxidation period the dissolved silica increased from 1200 to 1800 μM and then silica at the beginning of the last reduction decreased back to 1200 μM.

The Fe-cycling experiments with an initial Fe(II) concentration of 1 mM showed overall similar trends regarding silica mobility as the 0.5 mM Fe(II) experiments (Fig. S1).

3.1.5. Influence of silica on cell-mineral interactions during Fe redox cycling at low Fe concentrations

At the end of the three subsequent Fe redox cycles, solid phases were analyzed with SEM. The cocci-shaped, ~1 μm *Synechococcus* sp. PPC 7002 cells showed no signs of encrustation with Fe minerals, neither in the 'no silica' nor in the 'low silica' setups, while the rod-shaped *S. colwelliana* cells were present at much lower number, also not encrusted (Fig. 3). The mineral phases all appeared poorly crystalline, and the aggregates reached sizes of 0.5–8 μm. Cell morphology and crystallinity of the minerals were similar in 'no silica' and 'low silica' setups. SEM images of samples taken from the 1 mM Fe experiments at the end of the third reduction half-cycle revealed similar structure and aggregates as the samples from the 0.5 mM Fe experiments (Fig. S3). Specifically, we observed poorly crystalline minerals in the 'no silica' and 'low silica' setups as described for the 0.5 mM Fe(II) experiment and the cells were mostly free of encrustation but formed aggregates with the minerals.

3.1.6. Influence of silica on mineralogy during Fe redox cycling at low Fe concentrations

After each half-cycle of the 0.5 mM Fe cycling experiments, we performed μXRD measurements; ^{57}Fe Moessbauer spectroscopy measurements were not possible with these samples due to the low amount of Fe. μXRD analysis of samples from 'no silica' and 'low silica' setups revealed the presence of mainly poorly crystalline mineral phases, although the products from the 'no silica' setups might contain traces of goethite and vivianite and/or lepidocrocite (Fig. 3). Samples from the 'high silica' setups, in contrast, contained vivianite and/or lepidocrocite, as well as magnetite after the first cycle. With ongoing redox cycling the mineral crystallinity decreased in the 'high silica' setups.

The minerals collected from the 1 mM Fe(II) experiments (Fig. S2) showed higher crystallinity with ongoing cycling, but also with higher silica concentrations. After the second and third cycle, samples from the 'high silica' setup contained vivianite or lepidocrocite as well as potential traces of goethite, siderite and magnetite.

3.2. Effect of Si on iron cycling at high Fe concentrations (2.5 mM and 5 mM)

In these experiments, we also tracked total iron, $Fe(II)_{total}$ and dissolved silica concentration as well as cell counts for cyanobacteria and Fe(III)-reducing bacteria over three subsequent oxidation and reduction cycles (Fig. 5). This section focuses on the 2.5 mM Fe(II) experiments as these showed intense iron cycling (Fig. 5). The 5 mM Fe(II) experiments, in contrast, were dominated by struggling cells caused by iron toxicity effects; therefore, the respective data is provided in Fig. S4.

3.2.1. Influence of silica on Fe(II) oxidation and cell counts during Fe redox cycling at high Fe concentrations

In the 2.5 mM Fe(II) experiments, we found that the silica concentration strongly influenced Fe(II) oxidation. Fe(II) oxidation rates were much higher for the 2.5 mM Fe(II) experimental systems as compared to the 0.5 mM experiments (130–168 μM/day and 100 μM/day, respectively) (Fig. 6; Table S3). At the same time, Fe(II) oxidation rates in the first half-cycle were relatively similar regardless of the silica concentration (130–170 μM/day). Rather than oxidation rates, silica concentrations seem to impact the extent of Fe(II) oxidation: After 20 days, the Fe(II) oxidation in the 'no silica' and 'low silica' setups was complete (>99 %), but remained incomplete in the 'high silica' setups (~80 %) (Fig. 5A–C). With ongoing cycling the Fe(II) oxidation rates decreased in all experiments with 2.5 mM Fe(II). In the second half-cycle, Fe(II) in the 'no silica' and 'low silica' setups was nearly completely oxidized (>90 %) at rates of 12–55 μM/day. In 'high silica' setups, in contrast, oxidation rates were similar (5–50 μM/day), but the Fe(II) was only oxidized incompletely (20–60 %). During the third period, the 'no silica' and 'low silica' setups showed an Fe(II) oxidation extent of ~95 % (~200 μM, 1–9 μM/day), whereas the 'high silica' setup displayed incomplete Fe(II) oxidation (60 %; 19–72 μM/day).

Regardless of the silica concentration, the Fe-cycling experiments with 5 mM initial Fe(II) showed lower Fe(II) oxidation rates than the 2.5 mM Fe(II) experiments (maxima of 66 μM/day and 170 μM/day respectively; Table S3). In the 'no silica' and partly also in the 'low silica' setups, 60 % of the Fe(II) was oxidized in the first 40 days; subsequently the Fe(II)/$Fe_{(tot)}$ ratio fluctuated between 40 and 80 % during all half-

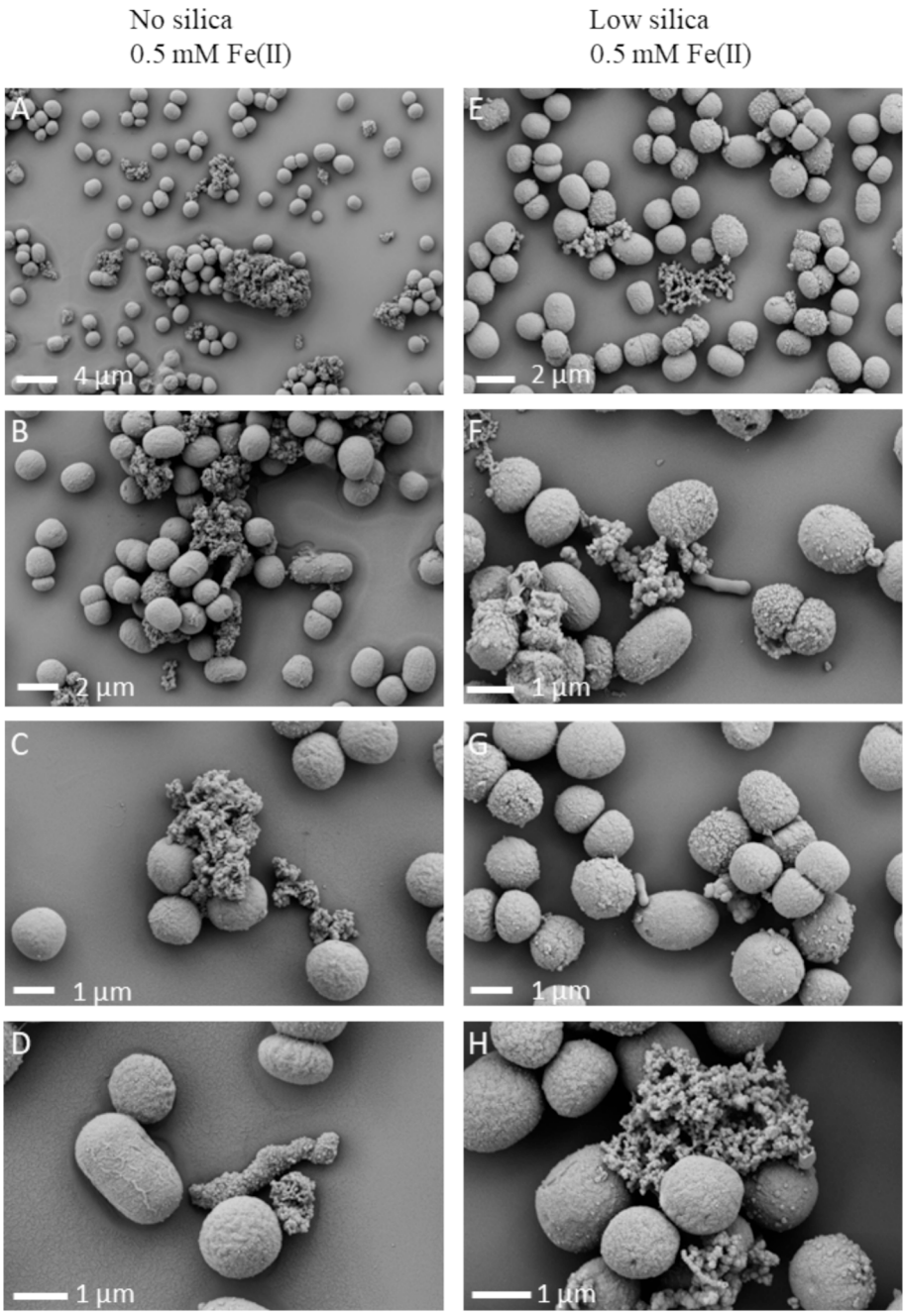

Fig. 3. SEM images of cell-mineral aggregates in samples taken from 0.5 mM Fe(II) cycling experiments (without added silica and in the presence of 0.67 mM silica) at the end of the third reduction half-cycle. The cocci-shaped 1 µm large bacteria are *Synechococcus* sp. PCC 7002, the smaller rod-shaped bacteria are *S. colwelliana*.

cycles (Fig. S4A, D, G B, E, H). In the 'no silica' setups, the cyanobacteria cell number reached $1*10^7$ cells/mL at the end of the first redox cycle and then decreased during the second oxidation half-cycle. Notably, the contents of the bottles did not turn green during these experiments. In contrast, in the 'high silica' setups, up to 80 % of the Fe(II) was oxidized in all oxidation half-cycles (Fig. S4C, F, I), the number of cyanobacterial cells increased to $3*10^7$ cells/mL, and the contents of the bottles turned green (Fig. 5).

3.2.2. *Influence of silica on O_2 production and cell counts during oxidative half-cycles at low Fe concentrations*

Different silica concentrations showed a strong influence on the accumulated oxygen concentrations. During the first, second and third Fe(II) oxidation half-cycles of the 'no silica' setups, oxygen concentrations reached up to 200, 400, and 150 µM respectively (Fig. 5A). In contrast, the 'low silica' setups showed only 100 µM oxygen in the first and second Fe(II) oxidation half-cycles, while in the third period oxygen increased to 300 µM (Fig. 5B). In the 'high silica' setup, oxygen concentrations were highest during the first oxidation half-cycle (600 µM) and appreciably lower in the second and third half-cycles (200 and 50 µM, respectively) (Fig. 5C).

The major impact of the silica concentration on cyanobacterial activity at high Fe(II) concentrations became apparent by the differences in color in the experimental bottles. In the 'no silica' setups, the contents of the bottles turned orange during the first half cycle and green during the second and third cycles (Fig. 5D). This contrasts with the 'low silica' setups where two bottles turned green only during the third half-cycle, and one bottle was constantly orange over the entire experiment

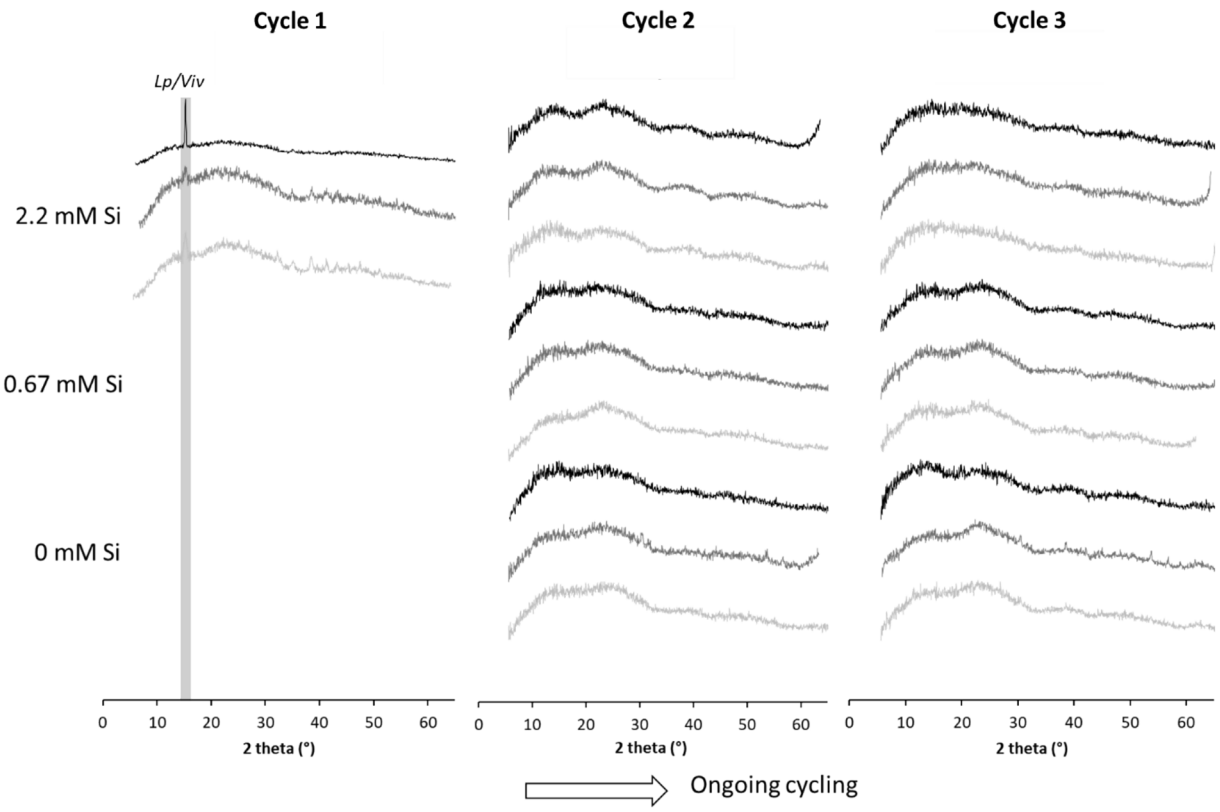

Fig. 4. μXRD patterns of the solids collected from the 0.5 mM iron experiment. The plots from left to right show the patterns after 1, 2 and 3 cycles from experiments performed without silica (bottom), with 0.67 mM added silica (middle) and 2.2 mM added silica (top). The triangles indicate reflections of the minerals vivianite (viv), lepidocrocite (lp), siderite (sd), magnetite (mg) and goethite (gt), respectively. All non-identified reflections were either low signal reflections of the defined mineral phases or instrumental background signal.

(Fig. 5E). Furthermore, the bottles of the 'high silica' setup turned green already during the first oxidation half-cycle (Fig. 5F). Cell counting revealed increasing densities of cyanobacteria cells with increasing silica concentrations. The maximum cell density reached $4*10^7$ cells/mL in all setups with different silica concentrations ('no silica', 'low silica' and 'high silica'). However, the time needed for bacterial growth varied: In the 'no silica' and 'low silica' setups, the growth phase lasted over 100 days, while in the 'high silica' setups, the maximum cell count was reached after 50 days.

The Fe-cycling experiments with 5 mM Fe(II) showed differences regarding oxygen accumulation compared to the 2.5 mM experiments. More specifically, in the 'no silica' setups, no O_2 was detected (Fig. S4A). This was also the case for the 'low silica' setups, except for one bottle with 400 μM O_2 in the second oxidation half-cycle (Fig. S4B). In the 'high silica' setups, oxygen was detected during all three oxidation half-cycles (400, 200 and 100 μM, respectively (Fig. S4C).

3.2.3. *Influence of silica on Fe(II) oxidation and cell counts during Fe redox cycling at high Fe concentrations*

With increasing silica, Fe(III) reduction rates increased as well, with maximum reduction rates of 11 μM/day in the 'no silica', 34 μM/day in the 'low silica' and 52 μM/day in the 'high silica' setups (Fig. 6; Table S4). In the first reduction half-cycle of the 'no silica' setups, Fe(III) reduction rates varied between 2–11 μM/day, and 30 % of the Fe(III) was reduced after ~80 days (Fig. 5A). In the second and third cycle, Fe (III) reduction rates decreased to 5–8 μM/day and 0.4–1.3 μM/day, respectively. The 'low silica' setups showed increasing Fe(III) reduction rates with ongoing cycling (maximum reduction rates of 15, 35 and 49 μM/day in the first, second and third cycle, respectively) (Fig. 5B). In the 'high silica' setups, the Fe(III) reduction rates were as high as 18–52 μM/day in the first reduction cycle, slightly decreased to 17–28 in the second cycle and were 17–41 μM/day in the third cycle (Fig. 5C).

In experiments with initially 5 mM Fe(II), the reduction rates and extent increased with increasing silica concentration, similar to the 2.5 mM Fe(II) systems (Fig. S4). During the third Fe(III) reduction half-cycle, the highest reduction rates of all experiments were measured (171 μM/day).

3.2.4. *Influence of silica concentration on Si mobility during Fe redox cycling at high Fe concentrations*

During Fe(II) oxidation, dissolved silica decreased, probably due to sorption to or co-precipitation with the formed Fe minerals, while silica went back into solution during Fe(III) reduction. The background silica in the 'no silica' setups (Fig. 5G) varied between 20 and 135 μM with a slight but continuous increase over time, not changing during iron cycling. In the 'low silica' setups (Fig. 5H), dissolved silica decreased during the first Fe(II) oxidation period and was associated with the solids completely after 50 days. During the first Fe(III) reduction half-cycle, silica was mobilized again. During the second and third Fe(II) oxidation period, up to 230 μM silica were associated with the solids, while during the second and third Fe(III) reduction periods, silica was dissolved again (maximum value of 670 μM). The 'high silica' setups (Fig. 5I) also showed how Fe(II) oxidation and Fe(III) reduction influenced silica mobility. During the first oxidation period, all silica was removed from solution within 50 days and was remobilized (1100 μM) during the first reduction half-cycle. With ongoing cycling, more silica remained in solution than in the first cycle, i.e. during the third Fe(III) reduction period 1730 μM silica was in solution. The silica mobility in the experiment with 5 mM Fe(II) was comparable to the 2.5 mM Fe(II) experiment (Fig. S4).

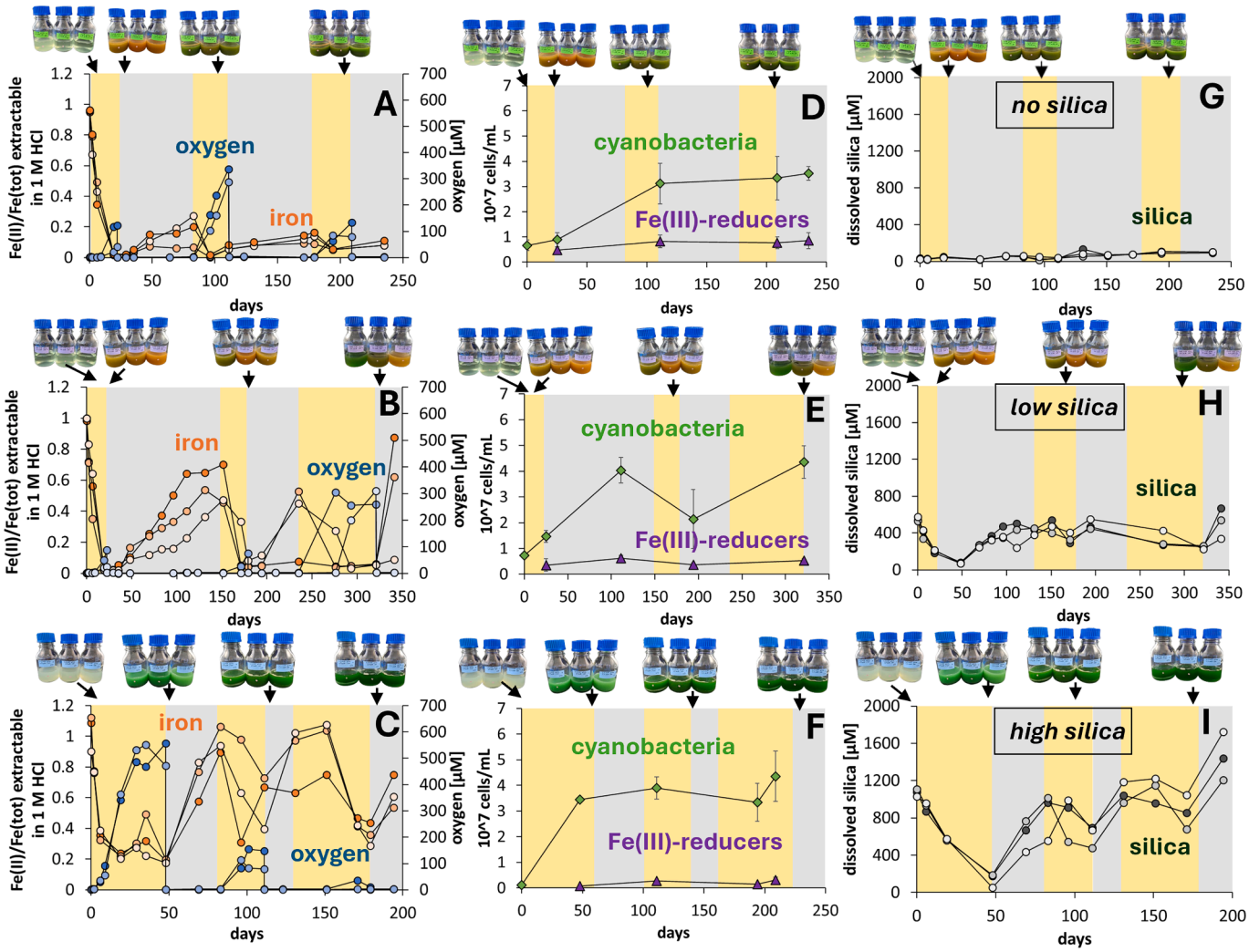

Fig. 5. Cycling experiments with 2.5 mM Fe(II) and 0, 0.67 and 2.2 mM added silica. Left panels show Fe(II)/$Fe_{(tot)}$ ratios (orange) and oxygen concentrations (blue). The panels in the middle column show cell counts (and standard deviation) of the cyanobacteria (green) and Fe(III)-reducers (purple) while the right columns show dissolved silica concentrations. The yellow background indicates periods of Fe(II) oxidation, while the grey background shows periods of Fe(III) reduction. The photographs on top show the triplicate bottles in the beginning of the experiment and at the end of each of the three oxidative half-cycles.

3.2.5. Influence of silica on cell-mineral interactions during Fe redox cycling at high Fe concentrations

At the end of each reduction cycle in the 2.5 mM Fe(II) experiments, samples were analyzed with SEM to investigate the cell-mineral interactions (Fig. 5). Samples from the 'high silica' setups at the end of the third Fe(III) reduction half-cycle showed much larger and more crystalline precipitates (up to 30 µm) than samples from the experiments with lower Fe(II) and lower silica concentrations (Fig. 7). The minerals exhibited a tabular 30 µm crystalline morphology; only few cells were visible. In the 'no silica' setups, all detected minerals showed low crystallinity and formed aggregates of a few µm in size. The cocci-shaped cyanobacterial cells in both the 'no silica' and 'high silica' setups formed aggregates with poorly crystalline minerals, while most cells were not encrusted, while a few cells (Fig. 7G) were partly encrusted. The smaller rod-shaped *Shewanella* cells were closely associated with the minerals, but generally free of encrustation.

3.2.6. Influence of silica on the mineralogy during Fe redox cycling at high Fe concentrations

The largest mineral particles found in the three replicates of the 'high silica' experiments with an initial Fe(II) concentration of 2.5 mM exhibited crossed tabular, bent tabular, and crossed needle-morphologies (Fig. 8). Based purely on optical observations, (A) resembles vivianite (Vuillemin et al., 2020; O'loughlin et al., 2021), and the bended structures in (B) and (C) resemble lepidocrocite (Antunes et al., 2014), whereas the crossed needles in (B) resemble goethite (Kaiser and Guggenberger, 2007; O'loughlin et al., 2021).

SEM-EDS analyses of minerals obtained at the end of incubation of the 'no silica' setups (2.5 mM iron) (Fig. 9B) revealed a high content of carbon, oxygen and iron. The iron and oxygen points towards Fe(III) (oxyhydr)oxides, and the carbon points towards EPS or bacterial cells. The particles collected from 'high silica' setups (2.5 mM iron) (Fig. 9C–E) showed different major elements: Fig. 9C revealed high concentrations of oxygen, iron and phosphorus. The iron, phosphorus and oxygen, as well as the tabular structure, point towards an Fe(II)

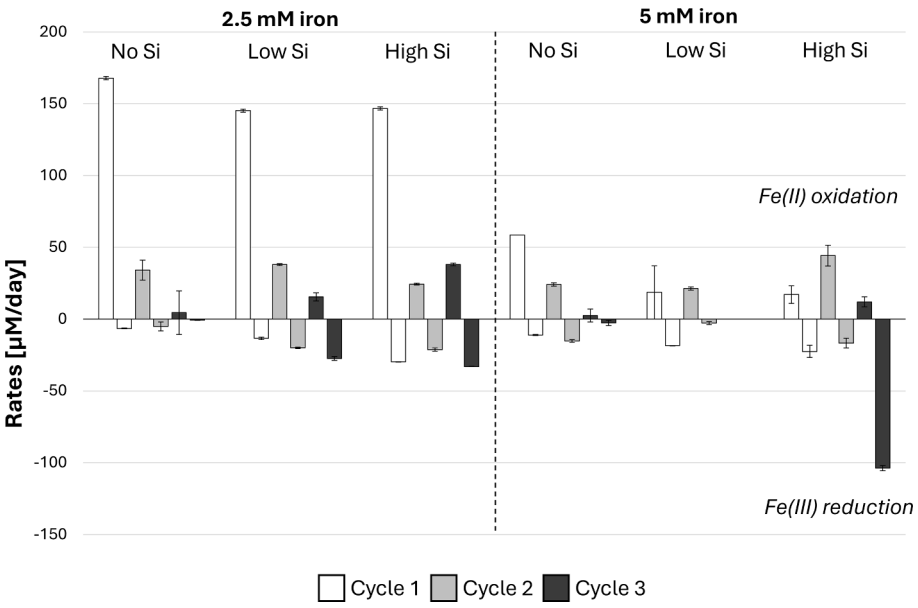

Fig. 6. Fe(II) oxidation (positive values) and Fe(III) reduction rates (negative values) in the three oxidative half-cycling experiments (white, grey, dark grey) with high initial Fe(II) concentrations (2.5 and 5 mM).

phosphate mineral (e.g. vivianite). In contrast, the sample shown in Fig. 9D is mainly composed of carbon, silica and oxygen, without no detectable iron present. Evidence for the co-precipitation of iron and silica is observed in Fig. 9E, where 2.6 % of silica with 4.2 % of iron were detected. These proportions closely resemble the results obtained under the 'high silica' setup with 1 mM iron (Fig. 9A).

With increasing silica concentrations, µXRD reflections became more distinct and sharper after all three reduction half-cycles, indicating an increasing crystallinity of the yielded minerals (Fig. 10), supporting the SEM observations. More specifically, samples from the 'no silica' setups showed only poorly crystalline minerals. In the 'low silica' setups, the (weak) reflections pointed towards siderite, goethite, vivianite, and magnetite. However, the prominent vivianite reflection at 15° 2-theta was missing, thus questioning whether this sample contains indeed vivianite. The most prominent reflection in all 'high silica' setups suggests the presence of vivianite, confirming the SEM-EDS results. This reflection, however, could also be interpreted as lepidocrocite. Additionally, we found indications for siderite, goethite and magnetite in the 'high silica' setups.

The µXRD results of the 5 mM Fe(II) experiment (Fig. S5), in contrast to the 2.5 mM Fe(II) experiment, showed crystalline minerals at all silica concentrations (Fig. 10). The higher the silica, the more reflections were visible. Again, we found indications for vivianite (Viv) and/or lepidocrocite (Lp), goethite (Gt), magnetite (Mag) and siderite (Sd).

3.2.7. Analysis of the solids collected from 5 mM iron experiments after three redox cycles using ^{57}Fe Moessbauer spectroscopy

Only one sample from a 2.5 mM Fe(II) 'no silica' experiment but all samples of the 5 mM experiments contained enough iron to collect Moessbauer spectra (Fig. 11). The hyperfine parameters can be found in Table S5. Due to the high cell densities and low iron concentrations, measurements of the low iron samples resulted in a poor signal-to-noise ratio, preventing appropriate processing of the spectra obtained. However, two Moessbauer spectra obtained after the oxidation of 1 mM Fe (II) by O_2 produced by cyanobacteria, measured at 77 K and 5 K, can be found in Fig. S6 and Table S6. Based on the hyperfine parameters data from both measurements pointed towards ferrihydrite (Byrne and Kappler, 2022).

The sample from the 'no silica'/2.5 mM iron experiment only exhibited a signal at 77 K (Fig. 11A), with a very dominant Fe(III) doublet (CS of 0.48 mm/s and QS of 0.84 mm/s) and a Fe(II) doublet (CS of 1.58 mm/s and QS of 2.8 mm/s). It is not possible to draw definite conclusions regarding the identity of the mineral phases from these data. However, the Fe(III) doublet points towards a poorly crystalline Fe(III) (oxyhydr)oxide, similar to what Gauger et al. (2016) found. The Fe(II) doublet points towards Fe(II) adsorbed to Si or organic carbon.

The measurements of samples from the 5 mM iron experiments showed significant differences depending on the silica concentrations present. The sample from the 'no silica' setups exhibited a defined sextet, a collapsed sextet and two doublets at 77 K (Fig. 11B). The defined sextet, which constituted 78.5 % of all phases, was characterized by a center shift (CS) of 0.49 mm/s, the quadrupole shift epsilon (ε) of −0.11 mm/s, and a hyperfine field (H) of 47.8 T), suggesting the presence of a crystalline Fe(III) (oxyhydr)oxide like goethite (Murad and Cashion, 2004). The collapsed sextet with an area of 8.1 % (CS of 0.50 mms/s, ε of −0.58 mm/s, H of 10 T), suggests the presence of a partly ordered poorly crystalline Fe(III) phase (Murad and Cashion, 2004). The narrow doublet which appeared with 2.9 % area shows a CS of 0.52 and a quadrupole splitting (QS) of 0.4, a clear indication of poorly crystalline Fe(III) (Cashion and Murad, 2012). The wider doublet with a CS of 1.4 mm/s and a QS of 2.8 mm/s suggested a poorly crystalline Fe(II) phase (Murad and Cashion, 2004).

At 5 K (Fig. 11C), the Fe(III) doublet ordered into two sextets, the Fe (II) doublet (CS of 1.01 mm/s and QS of 2.9 mm/s) (Cashion and Murad, 2012), however, was still visible. The Fe(II) doublet either points towards Fe(II) adsorbed to silica or to carbon (but not Fe(III) (oxyhydr) oxides). Additionally, we observed two defined sextets: one with an area share of 87.5 % (CS of 0.49 mm/s, ε of −0.11 mm/s and H of 49.5 T), one with an area of 10.2 % (CS of 0.59 mm/s, ε of −0.06 mm/s and H of 43.2 mm/s). Sextet 1 fitted very well to the defined sextet of the 77 K measurement and also indicates a crystalline Fe(III) (oxyhydr)oxide (e.g. goethite) (Murad and Cashion, 2004). Additionally, the collapsed sextet and Fe(III) doublet ordered at 5 K into the collapsed and partly into the defined sextet. The Fe(III) doublet therefore points towards ferrihydrite (Murad and Cashion, 2004), while the collapsed phase at 77 K points towards are more crystalline, very short-range ordered Fe(III) (oxyhydr) oxide such as lepidocrocite (Thompson et al., 2011; Chen and Thompson, 2021).

The 77 K spectrum of the 'low silica' sample (Fig. 11D) was dominated by a Fe(II) doublet (CS of 1.31 mm/s, QS of 2.43 mm/s) (Cashion

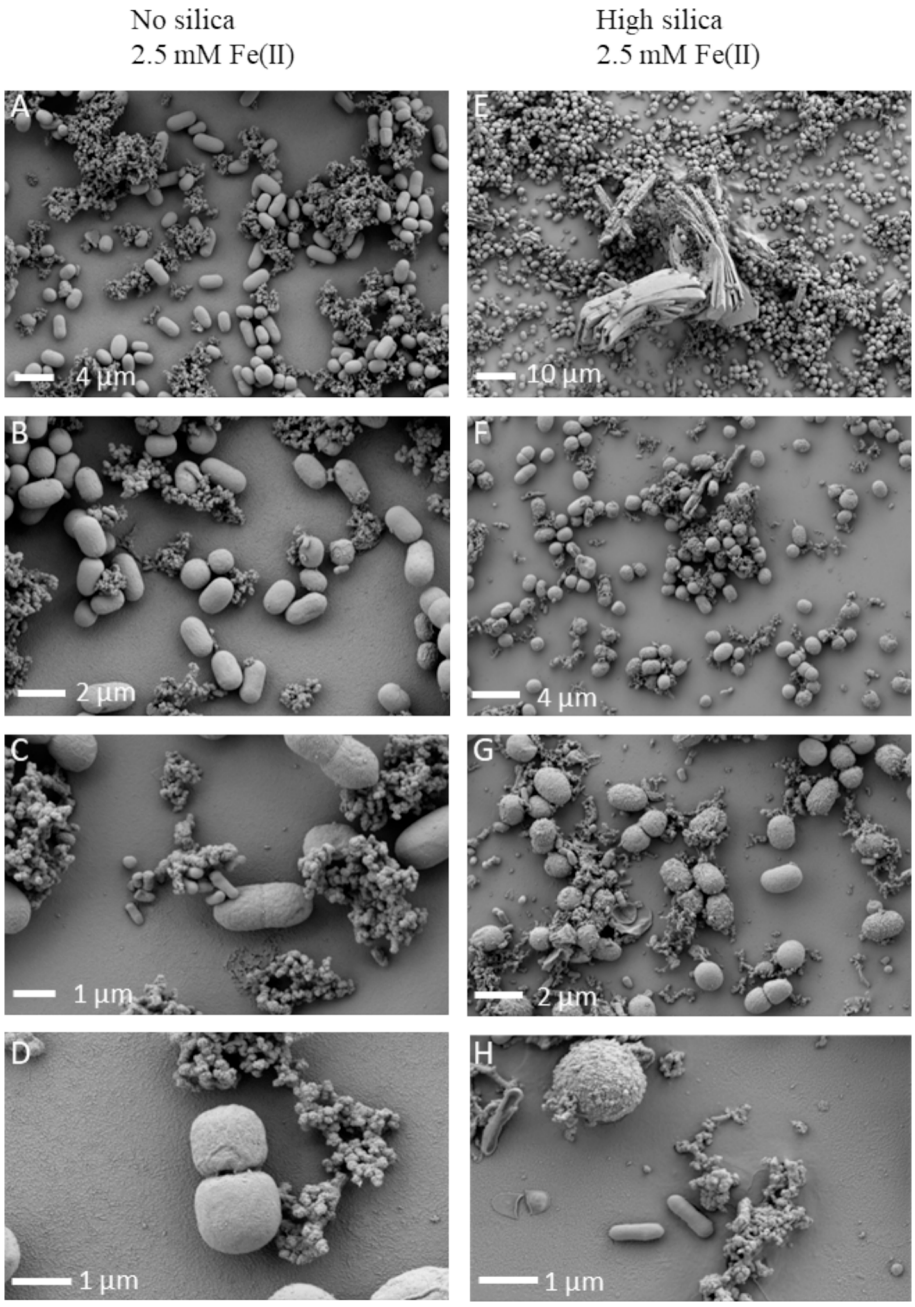

Fig. 7. SEM images of cell-mineral aggregates in samples taken from 2.5 mM Fe(II) cycling experiments (without added silica and in the presence of 2.2 mM silica) at the end of the third reduction half-cycle. The cocci-shaped 1 µm large bacteria are *Synechococcus* sp. PCC 7002, the smaller rod-shaped bacteria are *S. colwelliana*.

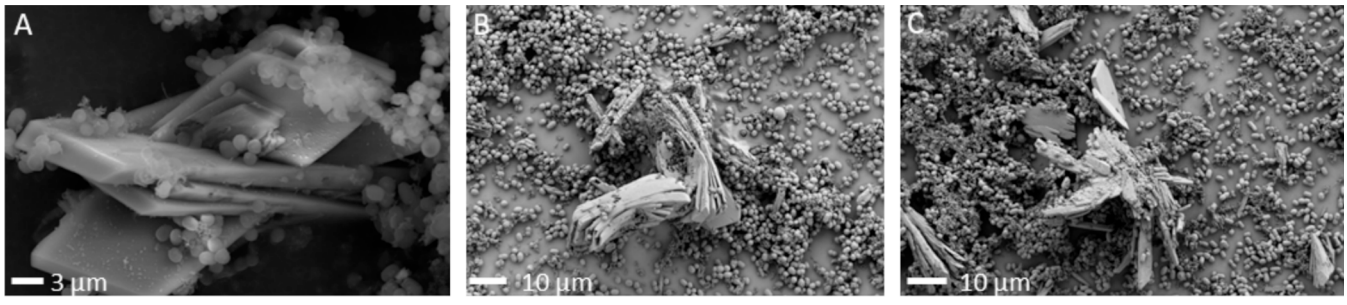

Fig. 8. SEM images of samples taken from the 2.5 mM Fe experiments with 'high silica' concentration. Images A, B, and C come from replicate bottles 1, 2 and 3.

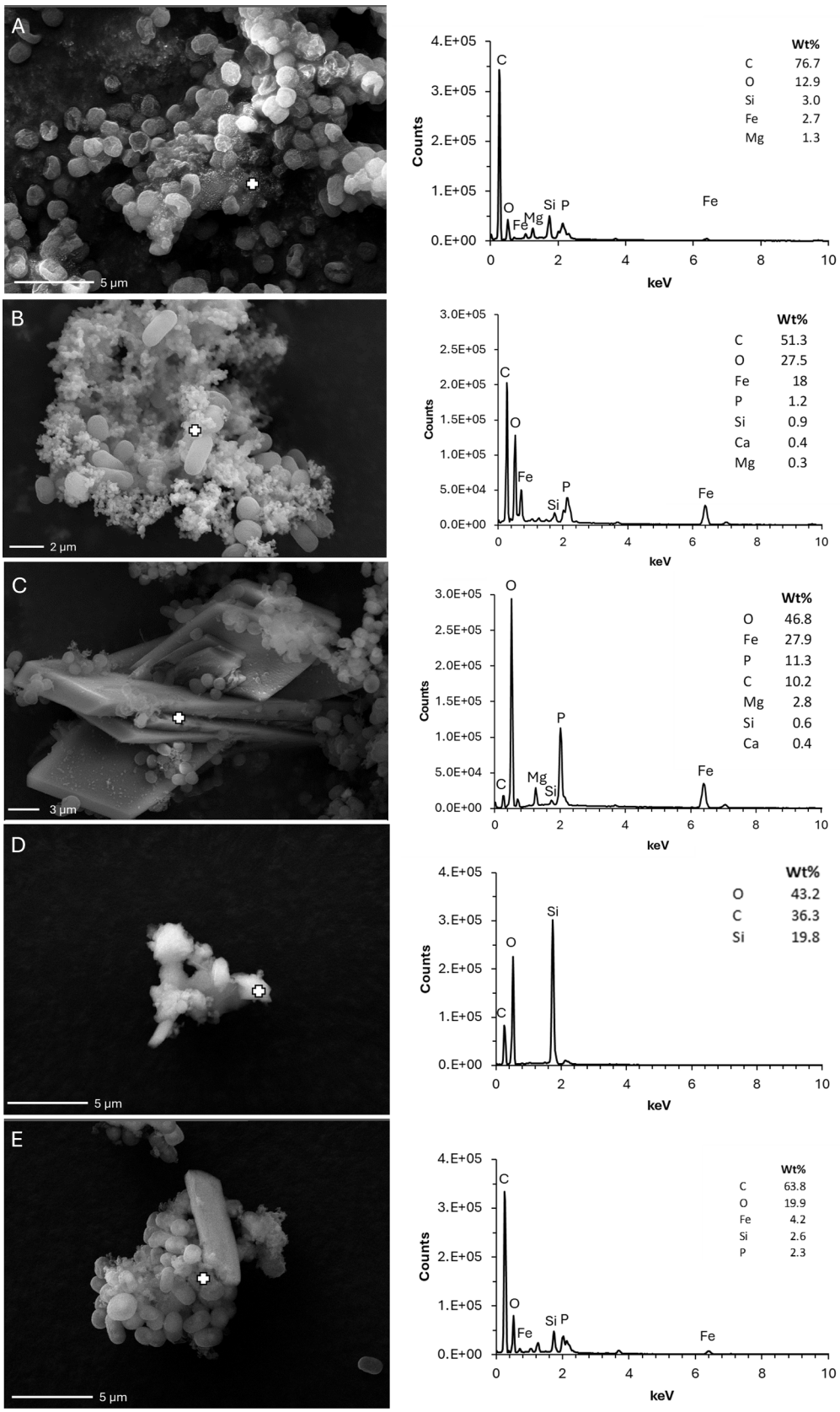

Fig. 9. EDS data of particles collected from an experiment with 1 mM Fe(II) and 2.2 mM silica (A), 2.5 mM Fe(II) with no silica (B) and 2.2 mM silica ('high silica') (C, D, E). The white cross indicates the spot where the EDS spectrum was measured.

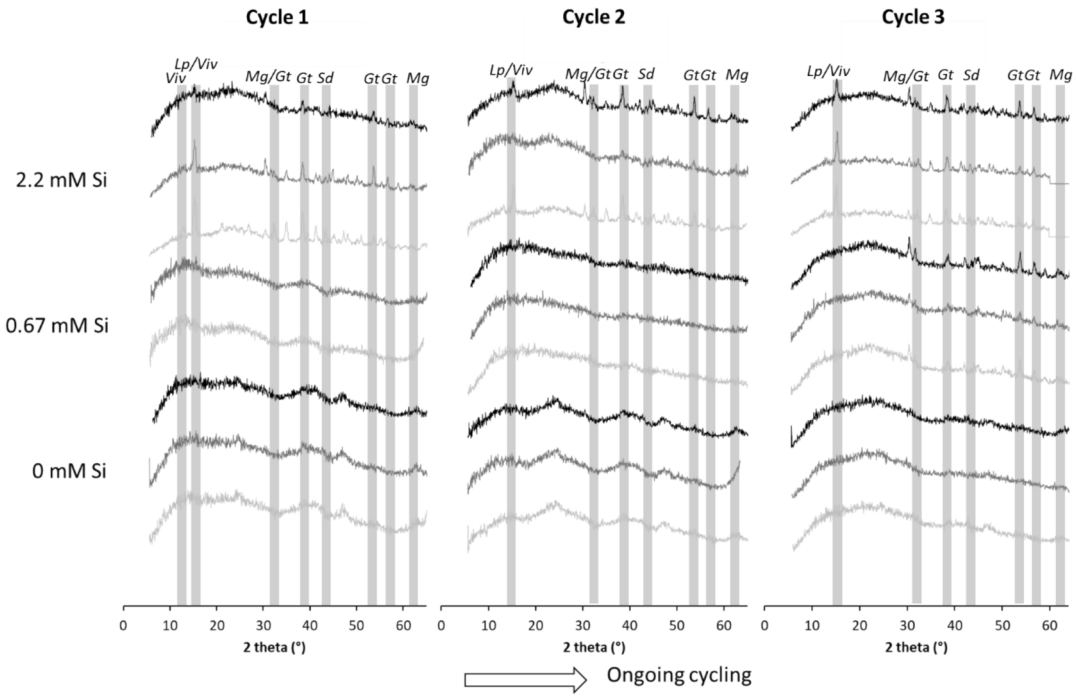

Fig. 10. μXRD patterns of the solids collected from the 2.5 mM iron experiment. The plots from left to right show the patterns after 1, 2 and 3 cycles from experiments performed without silica (bottom), with 0.67 mM added silica (middle) and 2.2 mM added silica (top). The triangles indicate reflections of the minerals vivianite (viv), lepidocrocite (lp), siderite (sd), magnetite (mg) and goethite (gt), respectively. All non-identified reflections were either low signal reflections of the defined mineral phases or instrumental background signal.

and Murad, 2012) and a defined sextet (CS of 0.49 mm/s, ε of 0.06 and H of 43.2 T). Additionally, a Fe(III) doublet (Cashion and Murad, 2012) was present (CS of 0.54 mm/s and QS of 0.65 mm/s). The doublets both represent a poorly crystalline phase, whereas the sextet again points towards a Fe(III) (oxyhydr)oxide of low crystallinity, such as poorly crystalline goethite (Thompson et al., 2011; Chen and Thompson, 2021).

The high background of the 5 K measurements (Fig. 11E) did not allow for a distinct differentiation of mineral phases. However, the features and parameters obtained pointed towards a defined and a collapsed phase. The defined sextet area increased from 32.0 to 59.5 % from the 77 K to the 5 K measurement. The majority of the Fe(III) doublet split into a defined sextet, which is typical for poorly crystalline Fe(III) (oxyhydr)oxides like ferrihydrite (Murad and Cashion, 2004), while 3.1 % remained as a Fe(III) doublet. A collapsed phase at 5 K points toward Fe(II) complexed with either silica or carbon, similar to Fe (II)-bearing clay minerals (see Latta et al., (2012)), indicating a mixture of poorly crystalline Fe(II)- and Fe(III)-bearing minerals.

Solids from the 'high silica' setups showed a very dominant Fe(III) doublet (CS of 0.48 mm/s and QS of 0.79 mm/s) combined with a Fe(II) doublet (CS of 0.89 mm/s and QS of 2.44 mm/s) at 77 K (Fig. 11F). However, we also observed the presence of a poorly crystalline Fe(III) (oxyhydr)oxide, for which the spectrum split into possibly multiple sextets at 5 K.

The dominant Fe(III) doublet at 5 K (Fig. 11G) can be explained by aggregation of Fe(III) with anions, such as silica or organic carbon (e.g. biomass-derived biomolecules including proteins/peptides or polysaccharides), which hindered the magnetic ordering (Thompson et al., 2011). The less dominant Fe(II) doublet exhibited at 5 K can also be explained by complexation of Fe(II) with silica, similar to Fe(II)-bearing silicates (see Latta et al. (2012)). Due to the high background noise, the 5 K measurement did not give further indication about the mineral identity.

In summary, the Moessbauer analyses of samples from the 'no silica' setups revealed crystalline goethite and poorly crystalline lepidocrocite, a small amount of ferrihydrite, and a poorly crystalline Fe(II) phase after the three cycles (Table 1). Measurements of solids from 'low silica' setups indicated Fe(II)-silica or Fe(II)-organic-carbon aggregates and poorly crystalline goethite and/or lepidocrocite. 'High silica' concentrations led to the formation of a very dominant magnetically unordered Fe(III)-phase (possibly short-range-ordered ferrihydrite), ferrihydrite and a low percentage of more crystalline Fe(III) (oxyhydr)oxides. We did not detect magnetite in all samples described.

4. Discussion

4.1. Influence of dissolved silica on iron mineralogy and crystallinity during microbial iron cycling

Key sources of silica in ancient oceans included weathering of emergent landmasses and hydrothermal processes in the oceanic crust, both delivering silica to continental shelves (Siever, 1992; Maliva et al., 2005). Much prior to the emergence and diversification of organisms forming siliceous hard parts (diatoms, radiolarians and sponges), chemical precipitation of Si-bearing minerals was the dominant Si sink (Medlin, 2016). Geochemical calculations suggest that residual dissolved silica concentrations in ancient oceans were around 0.67 mM (assuming precipitation of cristobalite (Maliva et al., 2005)) or 2.2 mM with amorphous silica minerals as the main precipitate (Siever, 1992). However, what is unknown is how elevated silica concentrations affected the mineralogy during ferric iron mineral precipitation and subsequent reduction by Fe(III)-reducers.

μXRD analysis of products from Fe cycling experiments showed that elevated silica concentrations enhance the crystallinity of iron minerals formed through abiotic Fe(II) oxidation by cyanobacterial O_2 coupled to microbial Fe(III) reduction. This is in contrast to the traditional view that associated silica inhibits the growth of crystalline iron minerals (Jones et al., 2009; Boglaienko et al., 2021; Nims and Johnson, 2022; Zhou et al., 2024). Two different processes may account for the observed mineral assemblages. First, in the absence of silica, ferrihydrite is the predominant iron mineral formed. In contrast, the presence of silica

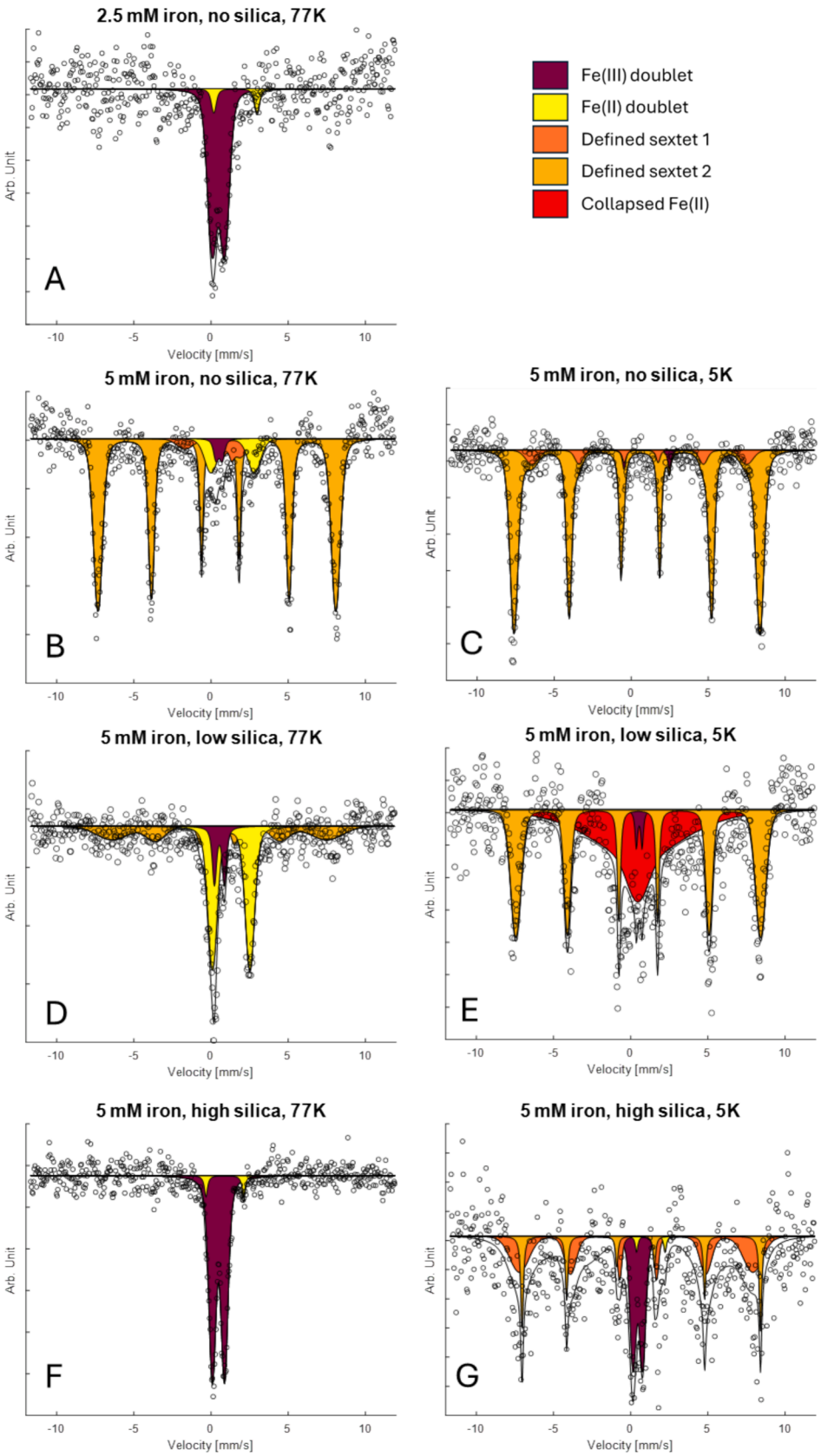

Fig. 11. ^{57}Fe Moessbauer spectra of solids collected from the 2.5 mM iron experiment without silica and from all 5 mM iron experiments after three subsequent cycles at 5 K and 77 K.

Table 1
Overview of the mineralogical results of ^{57}Fe Moessbauer spectroscopic analyses. The table shows the visible features in the obtained spectra at 77 K and 5 K and the most likely mineral based on the interpretation of these spectral features.

Sample	Features obtained at 77 K	Features obtained at 5 K	Most likely minerals*
1 mM iron, 'no silica'[x]	Fe(III) doublet	Defined sextet 1 Defined sextet 2	Ferrihydrite
2.5 mM iron, 'no silica'	Fe(III) doublet Fe(II) doublet	n.d.[#]	Poorly crystalline Fe(III) Fe(II) adsorbed to C_{org} or Si
5 mM iron, 'no silica'	Fe(III) doublet Fe(II) doublet	Defined sextet Fe(II) doublet	Ferrihydrite Fe(II) adsorbed to C_{org} or Si
	Defined sextet Collapsed sextet	Defined sextet Defined sextet	Goethite Lepidocrocite
5 mM iron, 'low silica'	Fe(III) doublet	Fe(III) doublet	Fe(III) adsorbed to C_{org} or Si
		Defined sextet	Ferrihydrite
	Fe(II) doublet	Collapsed Fe(II)	Fe(II) adsorbed to C_{org} or Si, Siderite?
	Defined sextet	Defined sextet	Goethite
5 mM iron, 'high silica'	Fe(III) doublet	Fe(III) doublet	Fe(III) adsorbed to C_{org} or Si
		Defined sextet	Ferrihydrite
	Fe(II) doublet	Fe(II) doublet	Fe(II) adsorbed to C_{org} or Si
		Defined sextet	Lepidocrocite
		Defined sextet	Nano-Goethite

* Moessbauer spectra oftentimes are not indicative of a specific mineral. Therefore, here we list the most likely mineral phases based on the observed Moessbauer spectral features. In the manuscript text further and more detailed explanations of the interpretations can be found.

x The spectra for the 1 mM iron experiment stem from preliminary Fe(II) oxidation experiments.

n.d. = not determined.

facilitates the formation of more crystalline minerals like goethite, lepidocrocite and siderite. In the 'high Si' setups, vivianite dominates the reflection spectra, consistent with findings from ferruginous lake sediments, where elevated silica concentrations have been shown to enhance vivianite precipitation (Vuillemin et al., 2020). Second, the increased crystallinity of iron minerals at higher silica concentrations might be due to greater Fe(III) microbial reduction under such conditions, which facilitates the formation of more stable mineral phases. Most silica went back to solution during Fe(III) reduction and was therefore no longer associated with the iron minerals (Fig. 5I). The higher extents of microbial Fe(III) reduction by *Shewanella oneidensis MR-1* in the presence of silica led to the formation of more crystalline iron minerals, probably stimulated by Fe(II)-catalyzed transformation of ferrihydrite to more crystalline Fe(III) (oxyhydr)oxides, such as lepidocrocite and goethite (Xiao et al., 2018). In addition, we observed that iron cycling at increasing Fe(II) concentrations (from 0.5 mM to 1, 2 and 5 mM iron) resulted in more crystalline minerals, corresponding to the findings from previous microbial Fe(III) reduction experiments (Glasauer et al., 2002; Wang et al., 2009) as well as observed for Fe(II)-initiated abiotic transformation of ferrihydrite to lepidocrocite and goethite (Boland et al., 2014). Furthermore, in a soil rich in short-range ordered goethite, repeated iron cycling at increasing iron concentrations (i.e., 1, 2.5 and 5 mM) resulted in a marginal increase in crystallinity, similar to laboratory microcosm experiments for repeated iron redox cycling (Thompson et al., 2006). In contrast, in our iron cycling experiment at realistic ancient ocean iron concentrations of 0.5 mM iron, we observed a higher crystallinity after only one oxidation–reduction cycle compared to the second and third cycle. At higher iron concentrations (1, 2.5 and 5 mM), we instead found a marginal increase in crystallinity with continued iron cycling.

In all samples from 'high silica' setups, as well as in several samples from the 'no silica' or 'low silica' setups at elevated iron concentrations of 2.5 and 5 mM, we found evidence after each redox-cycle for the formation of goethite and lepidocrocite (XRD, Moessbauer spectroscopy, SEM-EDS), ferrihydrite (Moessbauer), vivianite, magnetite and siderite (all XRD). In all systems containing silica, we also found evidence for the formation of Fe(II)- and Fe(III)-silica aggregates. In the following sections, we discuss how to interpret the presence of those Fe-silicate aggregates.

In our experiments at elevated iron and silica concentrations, all silica (in the 'high silica' setups up to 1600 μM) co-precipitated during Fe(II) oxidation (Fig. 5), with 1200–1600 μM silica dissolving again during iron(III) reduction. Different lines of evidence point to the formation of both Fe(II) silicates and to the presence of ferrihydrite-associated silica. At high silica concentrations, we observed incomplete Fe(II) oxidation at all iron concentrations suggesting the presence of stable Fe(II) silicates. Moessbauer spectroscopy analysis of solid phases at the end of the experiment – after the last reduction period in the 2.5 mM iron experiments – suggested unordered Fe(III) at temperatures where ferrihydrite would typically be magnetically ordered (Byrne and Kappler, 2022). The formation of ferrihydrite crystal units can be hampered by silica and organic carbon (ThomasArrigo et al., 2018), suggesting that one or both of these inhibited the magnetitic ordering of ferrihydrite.

The pH range in our experiments (7.0–7.5) is close to the pH range that favor the precipitation of Fe(II) silicates in anoxic environments (7.7–8.5) (Tosca et al. 2016) and 6.5 (Hinz et al., 2023). Prior to the addition of iron, vitamins and supplements, we filtered all visible white silica flocs out of the medium. Based on thermodynamic equilibrium calculations (not shown), our experimental conditions still favor the precipitation of up to 1 mM silica (cristobalite) in the 'high silica' setup with 5 mM Fe(II). Additionally, these calculations showed that the precipitation of up to 2.5 mM siderite in the 'high silica' setup with 5 mM Fe(II) is expected, while the precipitation of greenalite is not favored. It has to be noted, however, that other Fe(II)-silica gels, which are a variety of hydrated combinations of Fe(II) and silicate (SiO_2) (Tosca et al., 2016), are not covered in these equilibrium calculations due to missing solubility constants. Considering Moessbauer data demonstrating the presence of fully unordered Fe(II) in the sample collected after the last reduction period ('low silica', 5 mM iron) and the ratio of Fe(II) and Fe(III) in this sample (1:1), an aggregation of Fe(II) with silica seems most plausible. However, the geochemical framework is similar to the studies of Hinz et al. (2021, 2023), who microbially reduced 1 mM ferrihydrite in the presence of 1 mM at neutral pH and identified greenalite via transmission electron microscopy (TEM). We, however, did not use TEM in our study and therefore cannot rule out the presence of a small percentage of greenalite.

Our data suggest that most of the Fe(II) bound in Fe(II)-silica aggregates was still accessible for oxidation by O_2. During abiotic oxidation of Fe(II) by O_2 in the presence of phosphate and silica, Fe(III) phosphates were shown to precipitate prior to silicate-rich hydrous ferric oxides (Voegelin et al. (2010)). In the absence of phosphate, the ratio of dissolved silica to dissolved Fe(II) controlled the precipitation of minerals: at dissolved Si/dissolved Fe(II) ratios of ~0.5, a non-defined Fe(III) (oxyhydr)oxide was formed, at 0.5 to 0.1, 2-line ferrihydrite and at lower ratios lepidocrocite (Voegelin et al., 2010). Considering that our experiments were highly dynamic with fluctuating dissolved silica to iron ratios (Figs. 1 and 5), the presence of all the observed minerals in our samples (Figs. 4, 10 and 11) makes sense.

4.2. *Effect of Si on Fe cycling by cyanobacteria and Fe(III)-reducers*

Iron minerals in BIFs have an average oxidation state of +2.4 (Klein, 2005), corresponding to a $Fe(II)/Fe_{(tot)}$ ratio of ~0.4 or a Fe(II)/Fe(III) ratio of ~0.6. In our experiments, we found that in our most realistic scenario with 2.2 mM added silica and 0.5 mM iron, neither full Fe(II) oxidation nor (at least in two out of three reduction periods) full Fe(III) reduction was observed, in contrast to the 'no silica' and 'low silica'

setups, which showed full oxidation. For example, in our 'high silica' experiments with 0.5 mM Fe(II), the minerals formed after the first oxidation period maintained their Fe(II)/$Fe_{(tot)}$ ratio of 0.2 to 0.4 through the following reduction and oxidation periods. Later in the cycling experiment (after the third reduction) we obtained minerals with a stable Fe(II)/$Fe_{(tot)}$ ratio between 0.6 and 0.7. This indicates that the Fe(II)- and Fe(III)-bearing minerals obtained after several redox cycles were quite redox stable and have a Fe(II)/$Fe_{(tot)}$ ratio that is similar to the minerals present in BIF. In summary, based on the mineralogical analysis in our cycling experiments, we conclude that the presence of silica concentrations as estimated for the Archean oceans played a key role for the formation and preservation of mixed-valent (Fe(II)-/Fe(III)-bearing) iron minerals that also contain Fe-Si-minerals.

Our Fe cycling experiments showed that silica affected the cyanobacteria in various ways. For instance, the presence of silica was found to enhance cyanobacteria cell growth, resulting in an increased number of cells with increasing silica concentrations (Figs. 1 and 5). Additionally, cyanobacteria exhibited a more pronounced green coloration in the presence of silica compared to conditions lacking silica (Fig. 5), providing evidence for the formation of green photosynthetic pigments (chlorophyll *a* and carotenoids, especially synechoxanthin (Graham and Bryant, 2008)) which is an indicator for a general good viability and activity of the cells. Overall, we found that high silica concentrations mitigated the negative effect of Fe(II) on cyanobacteria (Swanner et al. (2015)). Specifically, the formation of aqueous Fe(II)-silica aggregates likely inhibited reactions between Fe(II) and O_2 that are known to produce harmful reactive oxygen species (Swanner et al. (2015), suggesting that silica may have played a protective role for cyanobacteria in early Earth's oceans.

4.3. *Silica in ancient oceans – effect on the formation of different Fe- and Si-minerals*

Typical minerals in the iron-rich BIF layers consist of hematite, magnetite, siderite and Fe(II) silicates, which have undergone diagenesis and metamorphism (Klein, 2005). Our experiments suggest that cyanobacteria, in conjunction with Fe(III)-reducers, can facilitate the formation of probable BIF precursor minerals (Krapež et al., 2003; Kappler et al., 2005; Konhauser et al., 2005). Such precursors were then subjected to various reactions in the water column and/or in the sediment (diagenesis) as well as to metamorphic processes (Konhauser et al., 2005). For instance, Fe(III) (oxyhydr)oxides formed in our experiments (e.g., ferrihydrite, goethite, lepidocrocite) can transform into the common BIF mineral hematite during diagenesis and metamorphism (Cudennec and Lecerf, 2005, 2006; Sun et al., 2015) as has been demonstrated in laboratory experiments using high-pressure/-temperature incubations (Köhler et al., 2013; Posth et al., 2013; Halama et al., 2016). Vivianite in our experiments formed because of the phosphate present in our microbial growth medium (367 μM). Since phosphate concentrations in Archean oceans were lower (values suggested range from 0.04-0.13 μM (Jones et al., 2015) up to 5.25 ± 2.63 μM (Konhauser et al., 2007)), vivianite was likely no typical BIF precursor mineral. In contrast, the formation of siderite in our experiments could indeed point towards its relevance for BIF. Siderite may form abiotically by precipitation of Fe^{2+} with the bicarbonate present in seawater, both stimulated by Fe(III) reduction coupled to organic matter oxidation by microorganisms. In our experiments at realistic ancient ocean Fe^{2+} concentrations of 0.5 mM (Holland, 1973; Morris, 1993), we calculated a possible siderite precipitation of 0.34 mM and a possible vivianite precipitation of 0.048 mM at the starting point of our experiment, before the initiation of Fe(II) oxidation (Table S7). This means that in our laboratory experiments, siderite and vivianite precipitation must be expected as soon as dissolved Fe^{2+} is present throughout the iron cycling, while under early-ocean-relevant phosphate concentrations of 0.04–0.13 μM (Jones et al., 2015), no vivianite is expected to precipitate.

One of the most interesting minerals that has been identified in BIF is the mixed-valent mineral magnetite, Fe_3O_4, which can be formed either via Fe(II) oxidation or Fe(III) reduction (Kappler et al., 2023). XRD analysis of the minerals formed in our cycling experiments showed only weak evidence for magnetite. Comparable iron cycling experiments with phototrophic Fe(II)-oxidizing and Fe(III)-reducing bacteria – to test iron mineral formation in the water column of the early ocean – similarly showed an absence of magnetite formation in cycling experiments (Schad et al., 2022). Furthermore, high-pressure/-temperature incubations (mimicking low-grade metamorphism of BIF precursor sediments after burial) of Fe(III) (oxyhydr)oxide minerals with biomass as reducing agent (Halama et al. (2016)) did not yield magnetite. In general, Fe(II) facilitates either 'solid-state conversion' from ferrihydrite to magnetite or dissolution-reprecipitation of ferrihydrite to goethite. However, the concentration of Fe(II) present, the Fe(II)/ferrihydrite ratio, and the Fe(II) formation rate all play a role in determining whether magnetite or goethite is precipitated. Based on previous experiments, lower Fe(II) concentrations and Fe(II) formation rates lead to the formation of goethite, while higher Fe(II) concentrations and Fe(III) reduction rates favor the formation of magnetite (Hansel et al., 2003, 2005). Kappler et al. (2023) demonstrated that microbial processes, particularly the activity of Fe(III)-reducing bacteria, enhance Fe(II) production, enabling biogenic magnetite formation even in systems with limited abiotic Fe(II) sources. Possible inorganic and organic ligands present in our experiments, such as phosphate, silica, or natural organic matter, however, can inhibit this 'solid-state conversion' by blocking the reactive surface of the ferrihydrite, similar to the effect of biogenic organic matter on ferrihydrite transformation (Han et al., 2020). Specific reasons for the low content or even absence of magnetite formation in our iron cycling experiments can be the slow Fe(III) reduction and the resulting low Fe(II) formation rates and extent in all our experiments. Hansel et al. (2003) found magnetite only in experiments with Fe(II)/ferrihydrite ratios greater than 1.0 mmol Fe(II)/g ferrihydrite. Piepenbrock et al. (2011) did not observe magnetite production with ferrihydrite concentrations below 5 mM and a minimum fraction of 25–30 % of Fe(II) of the total iron, independent of organic matter concentrations. This, in turn, means that the magnetite in BIF must have formed microbially with higher Fe(III) reduction rates than in our experiments. In our cycling experiments, the present phosphate, as well as possibly silica, concentrations adsorbed to ferrihydrite to a considerable extent thus inhibiting the solid-state transformation. An alternative magnetite formation pathway relevant for BIF was found by Hinz et al. (2023) who observed abiotic magnetite transformation from $Fe^{II/III}$-silicates like greenalite and cronstedtite at temperatures ≤150 °C at the seafloor during diagenesis. Li et al. (2017) similarly showed magnetite formation via a green rust intermediate when hot (>50 °C) hydrothermal fluids enriched in dissolved Fe(II) reacted with settling Fe(III) (oxyhydr)oxide particles.

The incomplete Fe(II) oxidation observed in various silica-containing setups (Figs. 1 and 5) in combination with the Moessbauer spectroscopy results (Fig. 11) indicated the presence of Fe(II) silicates. However, these Fe(II) silicates did not appear in the μXRD diffractograms, indicating low crystallinity. Key geochemical parameters in our 0.5 mM iron/'high silica' (2.2 mM) experiments (Fe and Si, pH) are similar to those assumed for the ocean during the Archean-Proterozoic transition, implying that such Fe(II)-Si aggregates could also have formed in the water column at that time. However, the Fe-Si-phases in our experiments were collected by filtration, and our data suggests that with ongoing cycling the majority of Fe(II) remained accessible to abiotic oxidation by O_2, while silica dissolved back. Thus, while Fe(II) silicates may have formed temporarily in the water column of the Archean ocean, they may have been oxidized during sedimentation and not deposited on the seafloor.

Moessbauer spectroscopy analysis of Fe(III) precipitates from our 'high silica' setups collected at the end of the oxidative periods indicated the presence of Fe(III) doublets, which point towards magnetically

unordered Fe(III) minerals. Since this was accompanied by distinct silica removal from solution, it suggests the formation of poorly crystalline Fe (III) minerals with sorbed or co-precipitated silicate. Similar processes could also have occurred in the Archean ocean, as proposed by Konhauser et al. (2007) and Fischer et al. (2009), who suggested that dissolved silica in the Archean ocean was adsorbed to Fe(III) (oxyhydr) oxide minerals. However, we observed that in the following reducing periods, most of the Fe(III)-associated silica returned to solution. This implies that the silica-Fe(III) associations were not stable, and instead the silicate became remobilized when the Fe(III) in these precipitates was reduced to Fe(II).

4.4. Implications of our laboratory Fe cycling experiments for the ecology and activity of cyanobacteria, photoferrotrophs and Fe(III)-reducers in early oceans

Previous studies have explored the ecological role of cyanobacteria in oceans during the Archean-Proterozoic transition, distinguishing between benthic cyanobacteria in shallow coastal areas and planktonic cyanobacteria in the open ocean. Planktonic cyanobacteria are hypothesized to be located at the surface of the water column, forming oxygen-rich oases (Olson et al., 2013), whereas benthic cyanobacteria would have been situated in shallow water, coastal environments (Sánchez-Baracaldo and Cardona, 2020). Anoxygenic phototrophic Fe (II)-oxidizing (photoferrotrophs) and Fe(III)-reducing bacteria, however, could have been situated in deeper anoxic water (Kappler et al., 2005). This distinction raises important questions regarding the biogeochemical cycling of iron in these environments, particularly concerning how much of the upwelled reduced iron was oxidized by the photoferrotrophs and how much of this iron was able to interact with the oxygen produced by cyanobacteria. With ongoing oxygenation of the oceans, the habitable zone of the photoferrotrophs likely decreased, making the interactions of Fe(II) with oxygen produced by cyanobacteria more relevant. One significant ecological advantage of cyanobacteria compared to photoferrotrophs is that they do not interact with the Fe(II) directly and are, therefore, less likely to be encrusted, as also evident in our SEM images.

It also remains to be investigated (1) whether the Fe(III)-bearing minerals formed during the interaction of dissolved Fe^{2+} with cyanobacterially produced O_2 can be reduced during sedimentation by Fe(III)-reducers within the water column, (2) whether the resulting dissolved Fe^{2+} can be re-oxidized again by photoferrotrophs, (3) how many redox cycles might take place during sedimentation through the water column to the seafloor, (4) how to distinguish if these metabolic processes took place in the water column versus the sediment pile, and (5) how these processes differed in coastal shallow settings compared to deeper waters and the open ocean. Our results indicate that at ancient-ocean-relevant iron (0.5 mM) and silica (2.2 mM) concentrations the minerals exhibit maximum crystallinity already after the first Fe cycling event. This implies that in an ancient ocean, even after just one cyanobacterial oxidation event, precursor Fe(III)-bearing BIF minerals can be generated, as postulated by previous work (Krapež et al., 2003; Kappler et al., 2005; Konhauser et al., 2005; Schad et al., 2022).

After the first Fe(III) reduction event in the experiments with the most ancient-ocean-relevant iron (0.5 mM) and silica (2.2 mM) concentrations, we found a variety of Fe(III)- and Fe(II)-bearing mineral phases, with an overall $Fe(II)/Fe_{(tot)}$ ratio of about 0.4, comparable to that of modern BIF (Klein, 2005). This $Fe(II)/Fe_{(tot)}$ ratio remained stable even after a further contact of the minerals with oxygen, pointing towards a certain redox stability. However, theoretically further reduction of the Fe(III) present in these minerals would have been possible, either in the deeper, anoxic water column or after sedimentation to the seafloor and accumulation in the sediment. Notably, in the presence of 2.2 mM silica, incomplete Fe(II) oxidation occurred, meaning that a mixture of Fe(II)- and Fe(III)-bearing phases associated with silica were present.

The sedimentation rates of ferrihydrite-cyanobacteria aggregates were experimentally determined by Li et al. (2024), who found for example rates of 3.82×10^{-4} cm/s in the presence 500 μM iron at pH 7. In a 400 m deep water column (proposed max. water depth on Archean-Proterozoic continental shelfs: (Trendall, 2002)), aggregates would remain ~132 days in suspension, leaving enough time to undergo Fe(III) reduction while settling. Reduction of Fe(III) is even possible in an oxic or microoxic water column inside of iron(III)-silica-aggregates, similar to marine snow (organic carbon aggregates formed in modern oceans) which show oxygen gradients from the outside to the inside of the particles (Alldredge and Cohen, 1987). The minerals being sedimented to the seafloor may ultimately undergo transformation at the seafloor and sediment pile through high pressure and temperature, resulting in the BIF mineralogy found today.

5. Conclusions

Our study demonstrates that the precursor minerals to BIF can be produced through microbial redox cycling by O_2-producing cyanobacteria and Fe(III)-reducing bacteria in the water column of an ancient ocean. The oxidation of Fe(II) initially resulted in the formation of poorly crystalline Fe(III) (oxyhydr)oxides, partially associated with silica, where a small extent of Fe(II) being associated with silica (Fe(II)-silica minerals) prevented complete Fe(II) oxidation. The following microbial Fe(III) reduction under anoxic conditions, either in deeper water layers in the ocean or inside of cell-mineral aggregates, led to the formation of Fe(II)-bearing minerals and a redissolution of some of the silica. Ultimately this would have resulted in mixed-valent mineral aggregates consisting of Fe(II), Fe(III) and silica minerals precipitating to the seafloor.

This suggests that for iron cycling between cyanobacteria and Fe(III)-reducing bacteria to occur in the water column, the water column must have been redox stratified. Before the GOE, we can assume that most of the oxygen produced by cyanobacteria was consumed by oxidation of dissolved Fe^{2+} in the photic zone, while near the shore or at the top of the water column, some Fe^{2+}-free oxygen oases may even have formed. However, large parts of the photic zone would also have remained oxygen-free, allowing close co-habitation with oxygen-sensitive phototrophic Fe(II)-oxidizers. As the oxygenation of the water by O_2 progressed, the role of phototrophic Fe(II)-oxidizers in the photic zone and their contribution to Fe(II) oxidation decreased, while the importance of cyanobacteria increased over time.

CRediT authorship contribution statement

Carolin L. Dreher: Writing – original draft, Visualization, Methodology, Investigation, Formal analysis, Data curation. **Manuel Schad:** Writing – review & editing, Validation, Funding acquisition, Conceptualization. **Jan-Peter Duda:** Writing – review & editing, Validation. **Stefan Fischer:** Writing – review & editing, Visualization, Data curation. **Jeremiah Shuster:** Writing – review & editing, Visualization, Data curation. **Yuhao Li:** Writing – review & editing, Visualization, Validation. **Kurt O. Konhauser:** Writing – review & editing, Supervision, Project administration, Funding acquisition, Conceptualization. **Andreas Kappler:** Writing – review & editing, Supervision, Resources, Project administration, Funding acquisition, Conceptualization.

Declaration of competing interest

The authors declare that they have no known competing financial interests or personal relationships that could have appeared to influence the work reported in this paper.

Acknowledgements

The authors would like to thank J. López Rivoldi and F. Kolb for their

experimental support. The authors would further like to thank F. Schädler and L. Grimm for maintenance and help in the laboratory. Dr. E. Runge, Dr. M. Maisch, Dr. P. Joshi, Dr. M. Mansor are acknowledged for fruitful discussions on experimental design and data interpretation.

This study was supported by the German Excellence Strategy of the German Federal and State Governments (EXC2124, 390838134; Tübingen Structural Microscopy Core Facility; A.K., S.F., J.S.). We would like to thank the Deutsche Forschungsgemeinschaft (DFG, German Research Foundation) for supporting grants for this project to AK, project ID AOBJ: 669932.

Appendix A. Supplementary material

The supplementary data contains the plots of the 1 mM and 5 mM datasets. Supplementary material to this article can be found online at https://doi.org/10.1016/j.gca.2025.07.023.

Data availability

Data are available through Mendeley Data at: https://doi.org/10.17632/g7nr34gvj9.1.

References

Alibert, C., 2016. Rare earth elements in Hamersley BIF minerals. Geochim. Cosmochim. Acta 184, 311–328.
Alldredge, A.L., Cohen, Y., 1987. Can microscale chemical patches persist in the sea? Microelectrode study of marine snow, fecal pellets. Science 235, 689–691.
Altermann, W., Kazmierczak, J., 2003. Archean microfossils: a reappraisal of early life on Earth. Res. Microbiol. 154, 611–617.
Antunes, R.A., Ichikawa, R.U., Martinez, L.G., Costa, I., 2014. Characterization of corrosion products on carbon steel exposed to natural weathering and to accelerated corrosion tests. Int. J. Corros. 2014, 1–9.
Bau, M., Möller, P., 1993. Rare earth element systematics of the chemically precipitated component in early precambrian iron formations and the evolution of the terrestrial atmosphere-hydrosphere-lithosphere system. Geochim. Cosmochim. Acta 57, 2239–2249.
Bekker, A., Holland, H.D., Wang, P.-L., Rumble, D., Stein, H.J., Hannah, J.L., Coetzee, L. L., Beukes, N.J., 2004. Dating the rise of atmospheric oxygen. Nature 427, 117–120.
Bekker, A., Planavsky, N., Rasmussen, B., Krapez, B., Hofmann, A., Slack, J.F., Rouxel, O. J., Konhauser, K.O., 2014. Iron formations: their origin and implications for ancient seawater chemistry. Treatise Geochem. 9, 561–628.
Beukes, N.J., 1984. Sedimentology of the kuruman and griquatown iron-formations, Transvaal supergroup, Griqualand West, South Africa. Precambr. Res. 24, 47–84.
Beukes, N.J., Gutzmer, J., 2008. Origin and paleoenvironmental significance of major iron formations at the Archean-Paleoproterozoic boundary. Rev. Econ. Geol. 15, 5–47.
Boglaienko, D., Qafoku, O., Kukkadapu, R.K., Kovarik, L., Katsenovich, Y.P., Cherkasov, D.E., Emerson, H.P., Levitskaia, T.G., 2021. Elemental iron: reduction of pertechnetate in the presence of silica and periodicity of precipitated nano-structures. Environ. Sci. Nano 8, 97–109.
Boland, D.D., Collins, R.N., Miller, C.J., Glover, C.J., Waite, T.D., 2014. Effect of solution and solid-phase conditions on the Fe(II)-accelerated transformation of ferrihydrite to lepidocrocite and goethite. Environ. Sci. Technol. 48, 5477–5485.
Braterman, P.S., Cairns-Smith, A.G., Sloper, R.W., 1983. Photo-oxidation of hydrated Fe2 +—significance for banded iron formations. Nature 303, 163–164.
Byrne, J.M., Kappler, A., 2022. A revised analysis of ferrihydrite at liquid helium temperature using Mössbauer spectroscopy. Am. Mineral. 107, 1643–1651.
Cairns-Smith, A.G., 1978. Precambrian solution photochemistry, inverse segregation, and banded iron formations. Nature 276, 807–808.
von Canstein, H., Ogawa, J., Shimizu, S., Lloyd, J.R., 2008. Secretion of flavins by shewanella species and their role in extracellular electron transfer. Appl. Environ. Microbiol. 74, 615–623.
Cashion, J.D., Murad, E., 2012. Mössbauer spectra of the acid mine drainage mineral schwertmannite from the Sokolov Basin, Czech Republic. In: Proceedings of the 36th annual condensed matter and materials meeting, Australia. ISBN: 978-0-646-57071-6.
Chen, C., Thompson, A., 2021. The influence of native soil organic matter and minerals on ferrous iron oxidation. Geochim. Cosmochim. Acta 292, 254–270.
Cloud, P., 1973. Paleoecological significance of the banded iron-formation. Econ. Geol. 68, 1135–1143.
Cloud, P., 1965. Significance of the gunflint (Precambrian) microflora. Science 148, 27–35.
Cudennec, Y., Lecerf, A., 2006. The transformation of ferrihydrite into goethite or hematite, revisited. J. Solid State Chem. 179, 716–722.
Cudennec, Y., Lecerf, A., 2005. Topotactic transformations of goethite and lepidocrocite into hematite and maghemite. Solid State Sci. 7, 520–529.
Czaja, A.D., Johnson, C.M., Beard, B.L., Roden, E.E., Li, W., Moorbath, S., 2013. Biological Fe oxidation controlled deposition of banded iron formation in the ca. 3770Ma Isua Supracrustal Belt (West Greenland). Earth Planet. Sci. Lett. 363, 192–203.
Czaja, A.D., Johnson, C.M., Roden, E.E., Beard, B.L., Voegelin, A.R., Nägler, T.F., Beukes, N.J., Wille, M., 2012. Evidence for free oxygen in the Neoarchean ocean based on coupled iron–molybdenum isotope fractionation. Geochim. Cosmochim. Acta 86, 118–137.
Dimroth, E., Chauvel, J.J., 1973. Petrography of the Sokoman iron formation in part of the central Labrador trough. Geol. Soc. Am. Bull. 84, 111–134.
Dreher, C.L., Schad, M., Robbins, L.J., Konhauser, K.O., Kappler, A., Joshi, P., 2021. Microbial processes during deposition and diagenesis of banded iron formations. Palaontologische Z. 95, 593–610.
Duda, J.-P., Thiel, V., Bauersachs, T., Mißbach, H., Reinhardt, M., Schäfer, N., van Kranendonk, M.J., Reitner, J., 2018. Ideas and perspectives: hydrothermally driven redistribution and sequestration of early Archaean biomass – the "hydrothermal pump hypothesis. Biogeosciences 15, 1535–1548.
Ernst, D.M., Bau, M., 2021. Banded iron formation from Antarctica: the 2.5 Ga old Mt. Ruker BIF and the antiquity of lanthanide tetrad effect and super-chondritic Y/Ho ratio in seawater. Gondw. Res. 91.
Fanning, K.A., Pilson, M.E., 1973. On the spectrophotometric determination of dissolved silica in natural waters. Anal. Chem. 45, 136–140.
Fischer, W.W., Schroeder, S., Lacassie, J.P., Beukes, N.J., Goldberg, T., Strauss, H., Horstmann, U.E., Schrag, D.P., Knoll, A.H., 2009. Isotopic constraints on the late Archean carbon cycle from the Transvaal Supergroup along the western margin of the Kaapvaal Craton, South Africa. Precambr. Res. 169, 15–27.
Garrels, R.M., Perry Jr., E.A., MacKenzie, F.T., 1973. Genesis of Precambrian iron-formations and the development of atmospheric oxygen. Econ. Geol. 68, 1173–1179.
Gauger, T., Byrne, J.M., Konhauser, K.O., Obst, M., Crowe, S., Kappler, A., 2016. Influence of organics and silica on Fe(II) oxidation rates and cell–mineral aggregate formation by the green-sulfur Fe(II)-oxidizing bacterium Chlorobium ferrooxidans KoFox – implications for Fe(II) oxidation in ancient oceans. Earth Planet. Sci. Lett. 443, 81–89.
Glasauer, S., Langley, S., Beveridge, T.J., 2002. Intracellular iron minerals in a dissimilatory iron-reducing bacterium. Science 295, 117–119.
Graham, J.E., Bryant, D.A., 2008. The biosynthetic pathway for synechoxanthin, an aromatic carotenoid synthesized by the euryhaline, unicellular cyanobacterium Synechococcus sp. strain PCC 7002. J. Bacteriol. 190, 7966–7974.
Halama, M., Swanner, E.D., Konhauser, K.O., Kappler, A., 2016. Evaluation of siderite and magnetite formation in BIFs by pressure–temperature experiments of Fe(III) minerals and microbial biomass. Earth Planet. Sci. Lett. 450, 243–253.
Halevy, I., Aleksker, M., Schuster, E.M., Popovitz-Biro, R., Feldman, Y., 2017. A key role for green rust in the Precambrian oceans and the genesis of iron formations. Nat. Geosci. 10, 135–139.
Halevy, I., Bachan, A., 2017. The geologic history of seawater pH. Science 355, 1069–1071.
Hamade, T., Konhauser, K.O., Raiswell, R., Goldsmith, S., Morris, R.C., 2003. Using Ge/Si ratios to decouple iron and silica fluxes in Precambrian banded iron formations. Geology 31, 35.
Han, T.-M., 1978. Microstructures of magnetite as guides to its origin in some Precambrian iron-formations. Fortschritte Mineral. 56, 105–142.
Han, T.-M., 1966. Textural relations of hematite and magnetite in some Precambrian metamorphosed oxide iron-formations. Econ. Geol. 61, 1306–1310.
Han, X., Tomaszewski, E.J., Sorwat, J., Pan, Y., Kappler, A., Byrne, J.M., 2020. Effect of microbial biomass and humic acids on abiotic and biotic magnetite formation. Environ. Sci. Technol. 54, 4121–4130.
Hansel, C.M., Benner, S.G., Fendorf, S., 2005. Competing Fe(II)-induced mineralization pathways of ferrihydrite. Environ. Sci. Technol. 39, 7147–7153.
Hansel, C.M., Benner, S.G., Neiss, J., Dohnalkova, A., Kukkadapu, R.K., Fendorf, S., 2003. Secondary mineralization pathways induced by dissimilatory iron reduction of ferrihydrite under advective flow. Geochim. Cosmochim. Acta 67, 2977–2992.
Harder, H., 1976. Nontronite synthesis at low temperatures. Chem. Geol. 18, 169–180.
Harder, H., 1978. Synthesis of iron layer silicate minerals under natural conditions. Clays Clay Miner. 26, 65–72.
Hartman, H., 1984. The evolution of photosynthesis and microbial mats: a speculation on banded iron formations. Microb. Mats Stromatolites 451–453.
Hegler, F., Posth, N.R., Jiang, J., Kappler, A., 2008. Physiology of phototrophic iron(II)-oxidizing bacteria: implications for modern and ancient environments: physiology of phototrophic iron(II)-oxidizing bacteria. FEMS Microbiol. Ecol. 66, 250–260.
Hinz, I.L., Nims, C., Theuer, S., Templeton, A.S., Johnson, J.E., 2021. Ferric iron triggers greenalite formation in simulated Archean seawater. Geology 49, 905–910.
Hinz, I.L., Rossi, L., Ma, C., Johnson, J.E., 2023. Simulated diagenesis of the iron-silica precipitates in banded iron formations. Am. Mineral. 108, 1732–1753.
Holland, H.D., 1973. The oceans: a possible source of iron in iron-formations. Econ. Geol. 68, 1169–1172.
Holland, H.D., 2002. Volcanic gases, black smokers, and the great oxidation event. Geochim. Cosmochim. Acta 66, 3811–3826.
Jacobsen, S.B., Pimentel-Klose, M.R., 1988. A Nd isotopic study of the Hamersley and Michipicoten banded iron formations: the source of REE and Fe in Archean oceans. Earth Planet. Sci. Lett. 87, 29–44.
Johnson, C., Beard, B., Weyer, S., 2020. The ancient earth. In: Johnson, C., Beard, B., Weyer, S. (Eds.), Iron Geochemistry: an Isotopic Perspective. Advances in Isotope Geochemistry. Springer International Publishing, Cham, pp. 215–360.
Johnson, C.M., Beard, B.L., Beukes, N.J., Klein, C., O'Leary, J.M., 2003. Ancient geochemical cycling in the Earth as inferred from Fe isotope studies of banded iron formations from the Transvaal Craton. Contrib. Miner. Petrol. 144, 523–547.

Johnson, J.E., Muhling, J.R., Cosmidis, J., Rasmussen, B., Templeton, A.S., 2018. Low-Fe (III) greenalite was a primary mineral from Neoarchean oceans. Geophys. Res. Lett. 45, 3182–3192.
Jones, A.M., Collins, R.N., Rose, J., Waite, T.D., 2009. The effect of silica and natural organic matter on the Fe (II)-catalysed transformation and reactivity of Fe (III) minerals. Geochim. Cosmochim. Acta 73, 4409–4422.
Jones, C., Nomosatryo, S., Crowe, S.A., Bjerrum, C.J., Canfield, D.E., 2015. Iron oxides, divalent cations, silica, and the early earth phosphorus crisis. Geology 43, 135–138.
Kaiser, K., Guggenberger, G., 2007. Sorptive stabilization of organic matter by microporous goethite: sorption into small pores vs. surface complexation. Eur. J. Soil Sci. 58, 45–59.
Kappler, A., Pasquero, C., Konhauser, K.O., Newman, D.K., 2005. Deposition of banded iron formations by anoxygenic phototrophic Fe(II)-oxidizing bacteria. Geology 33, 865–868.
Kappler, A., Thompson, A., Mansor, M., 2023. Impact of biogenic magnetite formation and transformation on biogeochemical cycles. Elements 19, 222–227.
Kasting, J.F., 1992. Models relating to Proterozoic atmosphere and ocean chemistry. In: Schopf, J.W., Klein, C. (Eds.), The Proterozoic Biosphere: A Multidisciplinary Study, Cambridge University Press, New York. pp. 1185–1187. ISBN-10: 0521366151.
Kendall, B., Lyons, T.W., Kaufman, A.J., Poulton, S.W., Anbar, A.D., 2010. Pervasive oxygenation along late Archaean ocean margins. Nat. Geosci. 3, 647–652.
Klein, C., 2005. Some Precambrian banded iron-formations (BIFs) from around the world: their age, geologic setting, mineralogy, metamorphism, geochemistry, and origins. Am. Mineral. 90, 1473–1499.
Klein, C., Beukes, N.J., 1992. Time Distribution, Stratigraphy, and Sedimentologic Setting, and Geochemistry of Precambrian Iron- Formations. In: Schopf, J.W., Klein, C. (Eds.), The Proterozoic Biosphere: A Multidisciplinary Study, Cambridge University Press, New York. pp. 139–146. ISBN-10: 0521366151.
Köhler, I., Konhauser, K.O., Papineau, D., Bekker, A., Kappler, A., 2013. Biological carbon precursor to diagenetic siderite with spherical structures in iron formations. Nat. Commun. 4, 1–7.
Konhauser, K.O., 2011. Chromium enrichment in iron formations record Earth's first acid rock drainage during the Great Oxidation Event. Nature 478, 369–373.
Konhauser, K.O., Hamade, T., Raiswell, R., Morris, R.C., Ferris, G.F., Southam, G., Canfield, D.E., 2002. Could bacteria have formed the Precambrian banded iron formations? Geology 30, 1079.
Konhauser, K.O., Lalonde, S.V., Amskold, L., Holland, H.D., 2007. Was there really an Archean phosphate crisis? Science 315, 1234.
Konhauser, K.O., Newman, D.K., Kappler, A., 2005. The potential significance of microbial Fe(III) reduction Fe (III) reduction in BIFs Blackwell Publishing Ltd ORIGINAL ARTICLE during deposition of Precambrian banded iron formations. Geobiology 3, 167–177.
Konhauser, K.O., Planavsky, N.J., Hardisty, D.S., Robbins, L.J., Warchola, T.J., Haugaard, R., Lalonde, S.V., Partin, C.A., Oonk, P.B.H., Tsikos, H., Lyons, T.W., Bekker, A., Johnson, C.M., 2017. Iron formations: a global record of Neoarchaean to Palaeoproterozoic environmental history. Earth Sci. Rev. 172, 140–177.
Krapež, B., Barley, M.E., Pickard, A.L., 2003. Hydrothermal and resedimented origins of the precursor sediments to banded iron formation: sedimentological evidence from the Early Palaeoproterozoic Brockman Supersequence of Western Australia. Sedimentology 50, 979–1011.
Krissansen-Totton, J., Arney, G.N., Catling, D.C., 2018. Constraining the climate and ocean pH of the early Earth with a geological carbon cycle model. PNAS 115, 4105–4110.
Lassak, J., Henche, A.-L., Binnenkade, L., Thormann, K.M., 2010. ArcS, the cognate sensor kinase in an atypical arc system of shewanella oneidensis MR-1. Appl. Environ. Microbiol. 76, 3263–3274.
Latta, D.E., Bachman, J.E., Scherer, M.M., 2012. Fe electron transfer and atom exchange in goethite: influence of Al-substitution and anion sorption. Environ. Sci. Technol. 46, 10614–10623.
Laufer, K., Nordhoff, M., Røy, H., Schmidt, C., Behrens, S., Jørgensen, B.B., Kappler, A., 2016. Coexistence of microaerophilic, nitrate-reducing, and phototrophic Fe(II) oxidizers and Fe(III) reducers in coastal marine sediment. Appl. Environ. Microbiol. 82, 1433–1447.
Lepot, K., 2020. Signatures of early microbial life from the Archean (4 to 2.5 Ga) eon. Earth Sci. Rev. 209, 103296.
Li, Y., Sutherland, B.R., Ilin, M.A., Schad, M., Robbins, L., Kappler, A., Yusta, I., Sánchez-España, J., Owttrim, G.W., Dreher, C., Smith, A.J.B., Alessi, D., Gringas, M.K., Konhauser, K., 2024. Cyanobacteria-ferrihydrite aggregates, BIF sedimentation and implications for Archaean-palaeoproterozoic seawater geochemistry. South Afr. J. Geol. 127, 359.
Li, Y.-L., Konhauser, K.O., Zhai, M., 2017. The formation of magnetite in the early Archean oceans. Earth Planet. Sci. Lett. 466, 103–114.
Maliva, R.G., Knoll, A.H., Simonson, B.M., 2005. Secular change in the Precambrian silica cycle: insights from chert petrology. Geol. Soc. Am. Bull. 117, 835–845.
Medlin, L.K., 2016. Evolution of the diatoms: major steps in their evolution and a review of the supporting molecular and morphological evidence. Phycologia 55, 79–103.
Mißbach, H., Duda, J.-P., van den Kerkhof, A.M., Lüders, V., Pack, A., Reitner, J., Thiel, V., 2021. Ingredients for microbial life preserved in 3.5 billion-year-old fluid inclusions. Nat. Commun. 12, 1101.
Morris, R.C., 1993. Genetic modelling for banded iron-formation of the Hamersley Group, Pilbara Craton, Western Australia. Precambr. Res. 60, 243–286.
Murad, E., Cashion, J., 2004. Iron Oxides. In: Mössbauer Spectroscopy of Environmental Materials and Their Industrial Utilization. Springer US, Boston, MA, pp. 159–188.
Nims, C., Johnson, J.E., 2022. Exploring the secondary mineral products generated by microbial iron respiration in Archean ocean simulations. Geobiology 20, 743–763.
O'loughlin, E.J., Boyanov, M.I., Gorski, C.A., Scherer, M.M., Kemner, K.M., 2021. Effects of Fe (III) oxide mineralogy and phosphate on Fe (II) secondary mineral formation during microbial iron reduction. Minerals 11, 149.
Olson, S.L., Kump, L.R., Kasting, J.F., 2013. Quantifying the areal extent and dissolved oxygen concentrations of Archean oxygen oases. Chem. Geol. 362, 35–43.
Percak-Dennett, E.M., Beard, B.L., Xu, H., Konishi, H., Johnson, C.M., Roden, E.E., 2011. Iron isotope fractionation during microbial dissimilatory iron oxide reduction in simulated Archaean seawater. Geobiology 9, 205–220.
Perry, E.C., Tan, F.C., Morey, G.B., 1973. Geology and stable isotope geochemistry of the Biwabik Iron Formation. Econ. Geol. 68, 1110–1125.
Piepenbrock, A., Dippon, U., Porsch, K., Appel, E., Kappler, A., 2011. Dependence of microbial magnetite formation on humic substance and ferrihydrite concentrations. Geochim. Cosmochim. Acta 75, 6844–6858.
Planavsky, N., Bekker, A., Rouxel, O.J., Kamber, B., Hofmann, A., Knudsen, A., Lyons, T. W., 2010. Rare Earth Element and yttrium compositions of Archean and Paleoproterozoic Fe formations revisited: new perspectives on the significance and mechanisms of deposition. Geochim. Cosmochim. Acta 74, 6387–6405.
Posth, N.R., Konhauser, K.O., Kappler, A., 2013. Microbiological processes in banded iron formation deposition. Sedimentology 60, 1733–1754.
Rasmussen, B., Krapez, B., Meier, D.B., 2014. Replacement origin for hematite in 2.5 Ga banded iron formation: evidence for postdepositional oxidation of iron-bearing minerals. Geol. Soc. Am. Bull. 126, 438–446.
Rasmussen, B., Krapež, B., Muhling, J.R., 2015a. Seafloor silicification and hardground development during deposition of 2.5 Ga banded iron formations. Geology 43, 235–238.
Rasmussen, B., Krapež, B., Muhling, J.R., Suvorova, A., 2015b. Precipitation of iron silicate nanoparticles in early Precambrian oceans marks Earth's first iron age. Geology 43, 303–306.
Rasmussen, B., Meier, D.B., Krapež, B., Muhling, J.R., 2013. Iron silicate microgranules as precursor sediments to 2.5-billion-year-old banded iron formations. Geology 41, 435–438.
Rasmussen, B., Muhling, J.R., Fischer, W.W., 2019. Evidence from laminated chert in banded iron formations for deposition by gravitational settling of iron-silicate muds. Geology 47, 167–170.
Reinhardt, M., Thiel, V., Duda, J.-P., Hofmann, A., Bajnai, D., Goetz, W., Pack, A., Reitner, J., Schanofski, M., Schönig, J., Whitehouse, M.J., Drake, H., 2024. Aspects of the biological carbon cycle in a ca. 3.42-billion-year-old marine ecosystem. Precambr. Res. 402, 107289.
Rico, K.I., Schad, M., Picard, A., Kappler, A., Konhauser, K.O., Mahmoudi, N., 2023. Resolving the fate of trace metals during microbial remineralization of phytoplankton biomass in precursor banded iron formation sediments. Earth Planet. Sci. Lett. 607, 118068.
Sánchez-Baracaldo, P., Cardona, T., 2020. On the origin of oxygenic photosynthesis and Cyanobacteria. New Phytol. 225, 1440–1446.
Schad, M., Byrne, J.M., ThomasArrigo, L.K., Kretzschmar, R., Konhauser, K.O., Kappler, A., 2022. Microbial Fe cycling in a simulated Precambrian ocean environment: implications for secondary mineral (trans)formation and deposition during BIF genesis. Geochim. Cosmochim. Acta 331, 165–191.
Schirrmeister, B.E., Gugger, M., Donoghue, P.C.J., 2015. Cyanobacteria and the Great Oxidation Event: evidence from genes and fossils ed. A. Smith. Palaeontology 58, 769–785.
Schirrmeister, B.E., Sanchez-Baracaldo, P., Wacey, D., 2016. Cyanobacterial evolution during the Precambrian. Int. J. Astrobiol. 15, 187–204.
Siever, R., 1992. The silica cycle in the Precambrian. Geochim. Cosmochim. Acta 56, 3265–3272.
Sun, S., Konhauser, K.O., Kappler, A., Li, Y.-L., 2015. Primary hematite in Neoarchean to Paleoproterozoic oceans. Geol. Soc. Am. Bull. 127, 850–861.
Swanner, E.D., Mloszewska, A.M., Cirpa, O.A., Schoenberg, R., Konhauser, K.O., Kappler, A., 2015. Modulation of oxygen production in Archean oceans by episodes of Fe(II) toxicity. Nat. Geosci. 8, 126–130.
ThomasArrigo, L.K., Byrne, J.M., Kappler, A., Kretzschmar, R., 2018. Impact of organic matter on iron(II)-catalyzed mineral transformations in ferrihydrite-organic matter coprecipitates. Environ. Sci. Technol. 52, 12316–12326.
Thompson, A., Chadwick, O.A., Rancourt, D.G., Chorover, J., 2006. Iron-oxide crystallinity increases during soil redox oscillations. Geochim. Cosmochim. Acta 70, 1710–1727.
Thompson, A., Rancourt, D.G., Chadwick, O.A., Chorover, J., 2011. Iron solid-phase differentiation along a redox gradient in basaltic soils. Geochim. Cosmochim. Acta 75, 119–133.
Tice, M.M., Lowe, D.R., 2004. Photosynthetic microbial mats in the 3,416-Myr-old ocean. Nature 431, 549–552.
Tosca, N.J., Guggenheim, S., Pufahl, P.K., 2016. An authigenic origin for Precambrian greenalite: implications for iron formation and the chemistry of ancient seawater. Bulletin 128, 511–530.
Trendall, A.F., 2002. The significance of iron-formation in the Precambrian stratigraphic record. Spec. Publ. Int. Assoc. Sedimentol. 33, 33–66.
Trendall, A.F., Blockley, J.G., 1970. The iron formations of the Precambrian Hamersley Group, Western Australia: with special reference to the associated crocidolite. Geol. Surv. West. Aust. 119, 336.
Van Kranendonk, M.J., 2011. Cool greenstone drips and the role of partial convective overturn in Barberton greenstone belt evolution. J. Afr. Earth Sci. 60, 346–352.
Voegelin, A., Kaegi, R., Frommer, J., Vantelon, D., Hug, S.J., 2010. Effect of phosphate, silicate, and Ca on Fe (III)-precipitates formed in aerated Fe (II)-and As (III)-containing water studied by X-ray absorption spectroscopy. Geochim. Cosmochim. Acta 74, 164–186.

Vuillemin, A., Friese, A., Wirth, R., Schuessler, J.A., Schleicher, A.M., Kemnitz, H., Lücke, A., Bauer, K.W., Nomosatryo, S., von Blanckenburg, F., Simister, R., Ordoñez, L.G., Ariztegui, D., Henny, C., Russell, J.M., Bijaksana, S., Vogel, H., Crowe, S.A., Kallmeyer, J., the Towuti Drilling ProjectScience team, 2020. Vivianite formation in ferruginous sediments from Lake Towuti, Indonesia. Biogeosciences 17, 1955–1973.

Walker, J.C.G., 1984. Suboxic diagenesis in banded iron formations. Nature 309, 340–342.

Wang, X.-J., Yang, J., Chen, X.-P., Sun, G.-X., Zhu, Y.-G., 2009. Phylogenetic diversity of dissimilatory ferric iron reducers in paddy soil of Hunan, South China. J. Soils Sedim. 9, 568–577.

Warke, M.R., Di Rocco, T., Zerkle, A.L., Lepland, A., Prave, A.R., Martin, A.P., Ueno, Y., Condon, D.J., Claire, M.W., 2020. The great oxidation event preceded a paleoproterozoic "snowball Earth. Proc. Natl. Acad. Sci. 117, 13314–13320.

Widdel, F., Schnell, S., Helsing, S., Ehrenreich, A., Assmus, B., Schink, B., 1993. Ferrous iron oxidation by anoxygenic phototrophic bacteria. Nature 362, 834–836.

Wu, L., Percak-Dennett, E.M., Beard, B.L., Roden, E.E., Johnson, C.M., 2012. Stable iron isotope fractionation between aqueous Fe(II) and model Archean ocean Fe–Si coprecipitates and implications for iron isotope variations in the ancient rock record. Geochim. Cosmochim. Acta 84, 14–28.

Xiao, W., Jones, A.M., Li, X., Collins, R.N., Waite, T.D., 2018. Effect of *Shewanella oneidensis* on the kinetics of Fe(II)-catalyzed transformation of ferrihydrite to crystalline iron oxides. Environ. Sci. Technol. 52, 114–123.

Zegeye, A., Bonneville, S., Benning, S.A., Fowle, D.A., Jones, C., Canfield, D.E., Ruby, C., MacLean, L.C., Nomosatryo, S., Crowe, S.A., Poulton, S.W., 2012. Green rust formation controls nutrient availability in a ferruginous water column. Geology 40, 599–602.

Zhang, H., Fu, H., Wang, J., Sun, L., Jiang, Y., Zhang, L., Gao, H., 2013. Impacts of nitrate and nitrite on physiology of shewanella oneidensis. PLoS One 8, e62629.

Zheng, X.-Y., Beard, B.L., Reddy, T.R., Roden, E.E., Johnson, C.M., 2016. Abiologic silicon isotope fractionation between aqueous Si and Fe(III)–Si gel in simulated Archean seawater: implications for Si isotope records in Precambrian sedimentary rocks. Geochim. Cosmochim. Acta 187, 102–122.

Zhou, A., Templeton, A.S., Johnson, J.E., 2024. Dissolved silica affects the bulk iron redox state and recrystallization of minerals generated by photoferrotrophy in a simulated Archean ocean. Geobiology 22, e12587.